

---

Mechanical Engineering Theses

Mechanical Engineering

---

Fall 11-17-2022

## AEROACOUSTIC ANALYSES FOR NOISE REDUCTION APPLICATION

Mahmoud M. Abdalmola  
*University of Texas at Tyler*

Follow this and additional works at: [https://scholarworks.uttyler.edu/me\\_grad](https://scholarworks.uttyler.edu/me_grad)



Part of the [Mechanical Engineering Commons](#)

---

### Recommended Citation

Abdalmola, Mahmoud M., "AEROACOUSTIC ANALYSES FOR NOISE REDUCTION APPLICATION" (2022).  
*Mechanical Engineering Theses*. Paper 21.  
<http://hdl.handle.net/10950/4136>

This Thesis is brought to you for free and open access by the Mechanical Engineering at Scholar Works at UT Tyler. It has been accepted for inclusion in Mechanical Engineering Theses by an authorized administrator of Scholar Works at UT Tyler. For more information, please contact [tgullings@uttyler.edu](mailto:tgullings@uttyler.edu).

AEROACOUSTIC ANALYSES FOR  
NOISE REDUCTION APPLICATION

by

MAHMOUD ABDALMOLA

A thesis submitted in partial fulfillment of the  
requirements for the degree of  
Master of Science in Mechanical Engineering  
Department of Mechanical Engineering

Tahsin Khajah, Ph.D., Committee Chair

College of Engineering

The University of Texas at Tyler  
November 2022

The University of Texas at Tyler  
Tyler, Texas

This is to certify that the Master's Thesis Dissertation of

MAHMOUD ABDALMOLA

has been approved for the thesis/dissertation requirement on

November 17 2022

For the Master of Science in Mechanical Engineering

Approvals:

DocuSigned by:

Tahsin Khajah

AC47690059AD419...

Thesis Chair: Tahsin Khajah, Ph.D.

DocuSigned by:

Nelson Fumo

9BAB5E76B5E14AE...

Member: Nelson Fumo, Ph.D.

DocuSigned by:

Alwathiqbellah Ibrahim

3A3F39F79FA8116...

Member: Alwathiqbellah Ibrahim, Ph.D.

DocuSigned by:

Nael Barakat

30D27AF79E60404...

Chair, Department of Mechanical Engineering

DocuSigned by:

M. K. Hammad

3E50E32BE8F046A...

Dean, College of Engineering

© Copyright by Mahmoud Abdalmola 2022  
All rights reserved

## Acknowledgement

First and Foremost, all praises and thanks to God, Most Gracious, Most Merciful, for his blessings, giving me the strength, peace of mind, and good health to finish this work.

I would like to express my deepest appreciation and gratitude to my supervisor and committee chair, Dr. Tahsin Khajah, for his continuous support. He continually conveyed a spirit of adventure and challenge, assistance and teaching. Without his care and guidance, nothing of this thesis would be possible.

It is a great pleasure to thank my committee members, Dr. Nelson Fumo and Dr. Alwathiqbellah Ibrahim, who supported and guided me with their insightful knowledge throughout my career.

I received tremendous support from many people, and their support made this thesis a reality.

I want to thank all of them. My colleagues and people who have willingly helped me: Mostafa, Atmeh, Ella, Abdullah, and Hesham.

I would also like to thank my Family: Mom, Dad, Nesreen, Daiana, Nermeen, Heba, and Nova, for their encouragement, which helped me finish this work. Special Thanks to my friend Reham, I owe you a lot. Thank you all!

## List of Figures

1	Basis functions for open, non-uniform knot vector $\Xi = \{0, 0, 0, 1, 2, 3, 4, 4, 5, 5, 5\}$ . . .	16
2	B-spline basis curve of order $p = 2$ was constructed using knot vector $\Xi = \{0, 0, 0, .5,$ $1, 1, 1\}$ . . . . .	17
3	B-spline surface of order $p = 2$ was constructed using the knot vectors $\Xi_1 = \{0, 0, 0, .5,$ $1, 1, 1\}$ and $\Xi_2 = \{0, 0, 0, 1, 1, 1\}$ along the first and second directions. . . . .	18
4	Difference between B-spline basis curve, NURBS curve and quarter circle constructed using same knot vector $\Xi = \{0, 0, 0, .5, 1, 1, 1\}$ . . . . .	20
5	Multi-patch geometry constructed from 5=simple simple patches . . . . .	21
6	Square geometry represented with a coarse mesh . . . . .	21
7	Square geometry after four levels of refinement . . . . .	22
8	Square geometry after eight levels of refinement . . . . .	23
9	Mesh for the proposed space with 2401 total number of elements. . . . .	32
10	The acoustic pressure distribution due to a sinusoidal signal with frequency $f =$ 10kHz applied at the center of a rectangular domain . . . . .	33
11	Pressure distribution at $t = 1.65E - 4$ s with ABC. . . . .	34
12	Pressure distribution at $t = 1.65E - 4$ s without ABC. . . . .	35
13	Pressure distribution at $t = 1.95E - 4$ s with ABC. . . . .	36
14	Pressure distribution at $t = 1.95E - 4$ s without ABC. . . . .	37
15	Pressure distribution at $t = 2.3E - 4$ s with ABC. . . . .	38
16	Pressure distribution at $t = 2.3E - 4$ s without ABC. . . . .	39

17	Evaluation of the acoustic pressure using homogeneous Neumann and first order ABC, for a point located at $(x_1, x_2) = (50 \text{ mm}, 25 \text{ mm})$ .	40
18	Velocity field for two co-spinning vortex	42
19	Acoustic sources field for two co-spinning vortex	44
20	Acoustic pressure field ( $Pa/m$ ) for the two co-spinning vortex for different times	45
21	Acoustic pressure $pa$ field for The two co-spinning vortex case	47
23	The decay of the acoustic pressure along the x-axis	50
24	The boundary conditions for the lid-driven cavity model.	51
25	Velocity field for Reynolds number 100 obtained only with $8 \times 8$ elements.	52
26	Axial velocity for different solutions against IGA using only $8 \times 8$ elements	53
27	Velocity and pressure fields for Reynolds number $Re = 5$ .	55
28	Velocity and pressure fields for Reynolds number $Re = 100$ .	56
29	Velocity and pressure fields for Reynolds $Re = 1000$ .	57
30	Velocity and pressure fields for Reynolds $Re = 10,000$ .	59
31	FEA element analysis solution for Reynolds number $Re = 100$ .	60
32	FEA element analysis solution for Reynolds number $Re = 1000$ .	61
33	CFD element analysis solution for Reynolds number $Re = 10000$ .	61
34	Affect of increasing Reynolds number on axial velocity at $x=0.5$ .	62
35	Affect of increasing Reynolds number on normal velocity at $y = 0.5 \text{ m}$ .	63
36	Schematic of wind tunnel problem	63
37	Mesh of wind tunnel problem	64
38	Velocity field at time $t=.01 \text{ s}$ for the flow passing through tunnel problem	65

39	Velocity field at time $t=.5$ s for the flow passing through tunnel problem . . . . .	65
40	Velocity field at time $t=1$ s for the flow passing through tunnel problem . . . . .	66
41	Harmonic acoustic sources generated from flow passing through tunnel . . . . .	67
42	Amplitude of acoustic sources generated from flow passing through tunnel . . . . .	68
43	Harmonic acoustic pressure generated from flow passing through tunnel . . . . .	69
44	Amplitude of acoustic pressure generated from flow passing through tunnel . . . . .	70
45	Schematic of wind tunnel problem with cylindrical object . . . . .	71
46	Velocity distribution over time before turbulence starts . . . . .	72
47	Velocity distribution over time after turbulence starts . . . . .	74
48	Mesh used for both Fluid and acoustic cases . . . . .	75
49	Time domain for acoustic force at point $x = .21$ . . . . .	76
50	Harmonic noise sources in $(Kg/s^2)$ for circular object case . . . . .	77
51	Amplitude of acoustic Pressure( $pa/m$ ) resulting from harmonic solution for circular object case . . . . .	78
52	Close image of the acoustic domain that shows the shape of the metamaterial . . . . .	80
53	Acoustic domain . . . . .	80
54	Interpolated acoustic sources( $Kg/s^2$ ) for the metamaterial domain . . . . .	81
55	Acoustic pressure amplitude ( $pa/m$ ) domain for the metamaterial . . . . .	82
56	Acoustic pressure amplitude ( $pa/m$ ) along the $x - axis$ for the three cases . . . . .	83

# Contents

Acknowledgement . . . . .	1
List of Figures . . . . .	1
Abstract . . . . .	7
<b>1 Introduction</b> . . . . .	<b>7</b>
1.1 Background . . . . .	7
1.2 Isogeometric Analysis . . . . .	8
1.3 Acoustic propagation schemes . . . . .	10
1.4 Metamaterials . . . . .	11
1.5 Fluid schemes . . . . .	12
1.6 Outline of the thesis . . . . .	14
<b>2 IGA - a brief introduction</b> . . . . .	<b>15</b>
2.1 B-spline basis function . . . . .	15
2.2 B-Spline curves and surfaces . . . . .	16
2.3 Non-Uniform Rational B-Splines . . . . .	17
2.4 Multi patch geometries . . . . .	19
2.5 Knot insertion . . . . .	20
<b>3 Strong and weak formulations</b> . . . . .	<b>22</b>
3.1 Finite Element formulation of Navier-stokes equations . . . . .	22
3.1.1 Pressure stabilization technique . . . . .	24

3.1.2	Modifications of the strong form . . . . .	24
3.2	Weak formulation . . . . .	25
3.3	Finite element formulation of Lighthill's acoustic analogy . . . . .	26
3.4	Strong and weak forms of the inhomogeneous wave equation . . . . .	26
3.4.1	Simulation of unbounded domains . . . . .	29
3.4.2	Time discretization . . . . .	30
3.5	Harmonic formulation . . . . .	30
<b>4</b>	<b>Validation</b>	<b>31</b>
4.1	ABC for wave equation . . . . .	31
4.2	Lighthill's acoustic analogy . . . . .	36
4.3	Solution to Navier-Stocks equations . . . . .	50
4.3.1	Lid-driven cavity flow . . . . .	51
<b>5</b>	<b>Applications</b>	<b>62</b>
5.1	Fluid-structure interaction analyses and computation of noise sources . . . . .	64
5.2	The effect of adding an obstacle inside the tunnel . . . . .	71
5.3	A metamaterial for aeroacoustic noise reduction . . . . .	79
<b>6</b>	<b>Conclusions</b>	<b>84</b>

## Abstract

In this study, we examine the hypothesis that airflow noise can be reduced by adding metamaterials. The introduction of any obstacle will generate more disturbance in the airflow and therefore add noise. Hence an efficient metamaterial design is required, capable of reducing noise even at higher flow disturbance. In order to examine this hypothesis, we developed a platform to perform isogeometric aeroacoustic analyses to solve Navier stokes equations first. We obtained the velocity fields from fluid-structure analyses and utilized the light-hill analogy to calculate the noise generated as a result of airflow. Then the Helmholtz equation was solved to perform wave propagation analyses using the calculated flow-induced source of the noise. Hence, the disturbance due to the introduction of the metamaterial was included in the analyses. The fluid-structure analyses were performed for the unsteady, in-compressible Naiver–Stokes problem to estimate velocity and pressure fields. The assumptions made can be viewed as Lid-driven cavity flow. The pressure stabilization technique was used for the treatment of the incompressibility constraint for unsteady flow cases. Results are obtained for a benchmark lid-driven cavity flow. The results were compared with published numerical and experimental finite element analysis studies for validation.

# 1 Introduction

## 1.1 Background

The noise level generated by the rapid passage of air has become an issue for urban communities[1]. Also, many machines generate a considerable amount of noise that reduces the quality of life [2]. At the same time, the government started to set regulations to restrict noise; many indus-

tries are moving towards machines with more acoustic comfort, which motivated the development of noise reduction strategies for example in aerospace and automobile industry. Primarily the engine noise was targeted by the researchers rather than the frame noise; therefore, the priority in noise reduction was given to the former. After the significant success in engine noise reduction over the past twenty-five years, considerable efforts have been made to reduce air-frame noise, and the field of computational aeroacoustics (CAA) has been actively utilized to achieve this goal [3]. Similarly, in the HVAC [4] industry, generally, the noise generated by the interaction between the air blown by the blower and the different components in the system such as flaps, thermal exchangers [5]. The common strategy to reduce the noise generated is to reduce the flow rates or increase the duct size which limit the noise generated and increase the customer comfort. One of the methods to attack noise problems is experimental methods [6]. However, several theories were developed to estimate the noise generated due to airflow and interaction with HVAC components. With the help of numerical methods [7], these theories could be tested and used reducing the need for experimental methods which are typically more expensive and time consuming. However, the existing theories face various challenges in physical and numerical aspects, such as scale disparity [8], simulation of unbounded domain [9], and reflection effects. Each Available aeroacoustics methodology addresses only some of these issues, making their accuracy dependent on the methodologies used.

## 1.2 Isogeometric Analysis

Isogeometric Analysis (IGA) is a rather new variation of classical Finite Element Analysis (FEA) with improved properties [10]. It has been developed to eliminate the gap between the worlds of

computer-aided design (CAD) and computer-aided engineering (CAE) as it combines the benefits of Finite Element Analysis (FEA) with the ability of exact and smooth representation of complex computational domains [11]. FEA is a numerical approximation technique that is widely used in computational mechanics. Recently, IGA has been used for various flow problems and proved its value within the field of fluid mechanics [12]. At first, some studies were conducted on steady-state in-compressible Stokes flow in lid-driven square cavity benchmark problem [13]. It was shown that IGA has many advantages in solving Navier–Stokes equation both in terms of providing higher continuity of state variables [14] and the ability to accurately represent complicated dynamic flow domains [15]. IGA was first introduced in [16],[17] to satisfy the need to improve Finite element analysis, which can be achieved to provide more accurate modeling of complex geometries and precisely represent common shapes like circles, and spheres and even more complex shapes, eliminating geometrical errors by representing exact geometry even at the coarsest level, as well as providing systematic refinements such as  $h$ ,  $p$ ,  $k$  and  $r$  refinements [18, 19].

In both conventional iso-parametric FEA as well as IGA the geometry of the computational domain and the solution spaces are represented using one set of basis functions. The CAD industry uses B-Splines, Non-Uniform rational B-Splines or T-spline to represent geometries. IGA adopts the basis functions used to develop CAD models to both represent the computational domain accurately and to represent the solution field. Both trial and test spaces in the discrete variation formulation of differential problems [11] are developed using these basis functions. As a result, IGA construct approximation spaces that exhibits higher regularity which is beneficial when compared to conventional FEA. Cottrell, Hughes, and Reali [20] demonstrated that the superior refinement and continuity IGA leads to a massive increase in accuracy of the estimated solution when per-

forming structural analyses using IGA [20]. It was also shown that accurate and smooth representation of the geometries enhances the accuracy of wave propagation analyses [21].

### 1.3 Acoustic propagation schemes

In 1952, The beginning of modern acoustics was considered by sir James Lighthill with two papers [22, 23], stating that the distribution of acoustic quadrupoles produces the sound field generated by a flow as a result of the instantaneous fluctuations of the velocity field in the flow, making him the first to develop the jet noise theory. followed by J. Ffowcs and D. Hawkings [24], they extend the work to include dipole and monopole distributions, defined as loading noise and thickness noise respectively. The force acting on the fluid determines the loading noise, whereas the geometry of the body determines the thickness noise. The potential of resolving this issue had been substantially aided by the emergence of high-performance computers. Equations involving the Navier-Stokes equation must be solved using a hybrid two-step procedure. First, by resolving Navier-Stokes equations, the turbulent flow field should be estimated. On the basis of the velocity fields discovered in the first stage, the source term is then determined. Finally, the calculated source's computed Wave or Helmholtz equations are used to estimate the acoustic pressure field. In the aerospace industry, significant noise reduction levels have already been attained with the use of contemporary computers and computational aeroacoustic techniques. Due to the imposition of stricter noise laws in numerous industries, including but not limited to the stricter noise regulations for the areas near airports, it still remains a difficult subject that requires additional development. In order to solve the flow field and the propagation of acoustic waves, respectively, the acoustic propagation and flow simulation are carried out using two different approaches.

It is often required to solve exterior acoustic problems when dealing with aeroacoustic analyses.

The IGA for exterior acoustic wave propagation was first developed by Khajah et al. [21, 25] and later combined with local refinement [26] and a novel absorbing boundary conditions (ABCs) which led to a highly accurate method to solve acoustic wave propagation analyses in IGA [27, 28]. IGA was compared to high order FEM in solving acoustic scattering problem [29]. It was shown that IGA suffer less from pollution error and provides considerably higher accuracy. Later, IGA was used to perform acoustic scattering problem in the context of On Surface Radiation Conditions [30] at dramatically low computational cost. IGA Collocation was later combined with high order ABCs [31]. IGA has been proved to be superior in shape optimization of acoustic devices as well [32–35]. It was shown that representing the boundaries with B-Spline may facilitate the design and optimization of acoustic devices [36].

Recently, IGA achieved significant success in a wide range of fields of computational mechanics especially when utilized to solve high-order partial differential equations (PDEs). Variational formulations of high-order PDEs such as Navier–Stokes require piecewise smooth and globally continuous basis functions. Conventional FEA have minimal continuity and losses accuracy when representing complex geometries [37]. The higher continuity of IGA, higher accuracy per degrees of freedom, and superior shape optimization possibilities makes a natural platform to perform aeroacoustic analyses.

## 1.4 Metamaterials

A metamaterial (MM) is a structure composed of one or many cells that together manipulate the wave in ways not possible using naturally occurring materials. A MM can manipulate the

wave in sub-wavelength regimes and may have a periodic or non-periodic design. Previous studies demonstrated the possibility of regulating waves using MMs [38, 39]. MMs were developed for elastic waves [39] similar to electromagnetic MMs [40–42] leading the way for rapid improvement for acoustic MMs. Initial studies were based on phononic crystal [38], but later on, Liu et al. [43] obtained a locally resonant unit by using a coating a high-density core with rubber which opened the door to studying acoustic MMs.

Recently, the concept of acoustic MMs has expanded. Torrent et al. suggested that any artificial acoustic structure that uses a repetitive or random structural unit to significantly modify the material’s equivalent acoustic parameters can be referred to as an ”acoustic metamaterial.” [44]. In 2012, Liang et al. theoretically obtained a broadband negative refractive index for a spatial folded structure [45]. They also realized double-negative parameters without using a local resonance mechanism, which compensated for the narrow bandwidth. In 2016, Maurya et al. extended spatially folded acoustic MMs into three dimensions [46]. Then the concept of 3D double-negative acoustic MMs was introduced and the broadband characteristics of such MMs were experimentally verified. In 2018, a spatial curl structure was demonstrated for reducing low-frequency aviation noise [47]. Khajah et al. demonstrated the possibility of tuning a acoustic MM for noise reduction and energy harvesting applications [36].

## 1.5 Fluid schemes

The mathematical theory and numerical methods for solving Navier–Stokes equations have a fundamental importance and demand a deep understanding in order to predict and control flow turbulence in nature and in technological applications [48]. Many phenomena that pique the inter-

est of scientists and engineers, such as combustion dynamics and manufacturing processes, are described by these equations as physical theories. When developing vehicles, aircraft, and power plants, Navier-Stokes equations are solved. They are also solved to analyze blood flow, pollution, and other phenomena. One of the most difficult issues to study is the numerical modeling of the unstable, viscous, incompressible Navier-Stokes equations. The classical Galerkin method may be affected from spurious oscillations when used to solve these equations [49].

Navier-Stokes equations are partial differential equations (PDS) that govern fluid flows and reflect a mass, momentum, and energy exchange. They are coupled and can only be solved analytically in a limited number of cases [50]. The turbulent behaviour of the fluid can be predicted by the dimensionless Reynolds number [51]. When solving these equations inside an irregular domain of complicated geometry with beginning and boundary conditions, numerical methods are necessary [50]. Stokes's equation needs to be solved using a method called "discretization," which turns PDEs into a system of algebraic equations. The goal is to get a numerical solution that is close to the real one.

Computational Fluid Dynamics(CFD) provides an approximate solution for the flow by solving the mathematical models [52, 53] through numerical methods. The most common methods used are Finite Volume Method (FVM) and FEM [52, 54, 55]. Direct Numerical Simulation (DNS) is the most powerful and accurate method to solve the turbulence flow. From its definition, the equation is solved without any approximation, filters, or modeling applied at the original governing PDEs [56], which can generate highly accuracy solutions but unfortunately, it also results in very high computational cost when conventional FEMs is used. As a result, it remains a preferred method but limited to low Reynolds numbers and rather simple geometries [57]. The sec-

ond common method used is Reynold Averaged Navier stokes (RANS) [58–60] which is an exciting approach. Rather than solving the original equations of Navier stokes, it adopts new filtered equations to be solved that are called the turbulence models [61] and it only solves the mean flow properties. Too many assumptions has to be made for the turbulence parameters for each problem [61]. As a result, RANS is not the first option to solve Navier Stock equations. Another method to solve these equations is Large Eddy Simulation (LES) which is used to solve turbulence flow [62]. In this method, the large scales are directly resolved, and the effect of the small scales on the large scales is modeled [63]. As a result, LES can be used to simulate turbulent flows with high Reynolds numbers and on complex geometry. Although it requires high computational cost, it is adopted by many researchers as one of the standard methods for computing the turbulent near field [64]. A detailed literature review of the current CFD methods used for CAA simulations can be found in [3].

## 1.6 Outline of the thesis

The remainder of the thesis is structured as follows: chapter one provides an introduction to the problem considered including the background and motivation, and provides a brief literature review on IGA, Acoustic propagation schemes, Metamaterials, and fluid schemes. The formulation of B-splines and NURBS in IGA is discussed briefly in Chapter two including the evaluation of curves and surfaces, calculation of Basis functions, basics of refinements, and analyses over multi-patch geometries. The strong and weak forms of the Navier stokes equation and discretization method are discussed, the finite element formulation of Lighthill’s equation, the strong and weak forms of the wave equation, and the simulation of the unbounded domain is discussed in

chapter three. The analyses performed in unbounded domains are validated in chapter four, and Lighthill's acoustic Analogy is validated in Chapter four. The numerical analyses of the flow are validated in four. The use of MMs for noise reduction is discussed in Chapter five to investigate the possibility of reducing Noise generated by airflow in a duct by adding a MM inside the duct. Finally, the result and future work are summarized and discussed in Chapter six.

## 2 IGA - a brief introduction

B-Splines and NURBS are used as the most common basis functions in IGA. A brief review of B-Splines and NURBS follows.

### 2.1 B-spline basis function

B-Splines are defined over a Knot vector which is a non-decreasing set of coordinates dividing the parameter space into elements. A knot vector  $\Xi$  can be written as  $\Xi = \{\xi_1, \xi_2, \dots, \xi_{n+p+1}\}$ , where  $\xi_i \in \mathbb{R}$  is the  $i^{\text{th}}$  knot,  $i$  is the knot index,  $i = 1, 2, \dots, n + p + 1$ ,  $p$  is the polynomial order, and  $n$  is the number of basis functions used to construct the B-spline curve. The equation that defines B-splines shows as follows, which is called the Cox-de boor formula.

$$N_{i,0}(\xi) = \begin{cases} 1 & \text{if } \xi_i \leq \xi < \xi_{i+1}, \\ 0 & \text{otherwise.} \end{cases} \quad (1)$$

For  $p = 1, 2, 3, \dots$ , they are defined by

$$N_{i,p}(\xi) = \frac{\xi - \xi_i}{\xi_{i+p} - \xi_i} N_{i,p-1}(\xi) + \frac{\xi_{i+p+1} - \xi}{\xi_{i+p+1} - \xi_{i+1}} N_{i+1,p-1}(\xi) \quad (2)$$

An example of constructing a basis function using the equations (1) and (2), is shown in Fig 1 for knot vector  $\Xi = \{\xi_1, \xi_2, \xi_3, \xi_4, \xi_5, \xi_6, \xi_7, \xi_8, \xi_9, \xi_{10}, \xi_{11}\} = \{0, 0, 0, 1, 2, 3, 4, 4, 5, 5, 5\}$  and degree of  $p = 2$ .

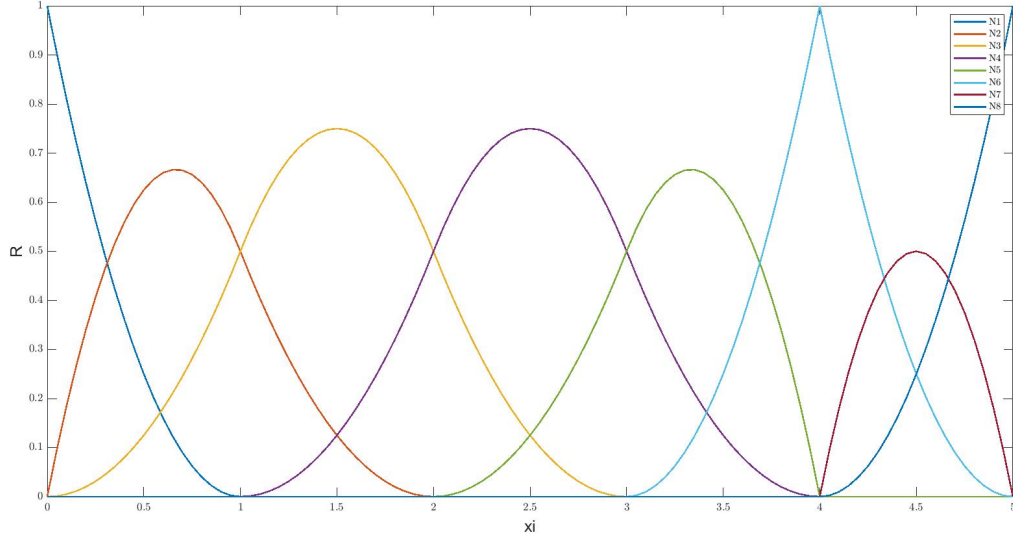


Figure 1: Basis functions for open, non-uniform knot vector  $\Xi = \{0, 0, 0, 1, 2, 3, 4, 4, 5, 5, 5\}$

## 2.2 B-Spline curves and surfaces

Similar to construction of basis functions in conventional FEA, B-spline curves are constructed by as a linear combination of B-splines basis functions. For instance a one-dimensional B-Spline curve is constructed as:

$$\mathbf{C}(\xi) = \sum_{i=1}^n N_{i,p}(\xi) \mathbf{B}_i, \quad (3)$$

where  $\{\mathbf{B}_i\}$ ,  $i = 1, 2, \dots, n$  is a set of control points. the basis function  $N_{i,p}$  is defined over the knot vector  $\Xi = \{\xi_1, \xi_2, \dots, \xi_{n+p+1}\}$  using the basis order  $p$ . A B-Spline curve defined using three

control points is shown in Fig.2. Similarly, a tensor product is used to construct a two-dimensional domain as;

$$\mathbf{S}(\xi, \eta) = \sum_{i=1}^n \sum_{j=1}^m N_{i,p}(\xi) M_{j,q}(\eta), \mathbf{B}_{i,j} \quad (4)$$

where  $\{\mathbf{B}_{i,j}\}$ ,  $i = 1, 2, \dots, n$ ,  $j = 1, 2, \dots, m$  is a given set of control points and  $p$  and  $q$  are the basis orders in first and second directions. The basis function  $N_{i,p}$  is defined over the knot vectors  $\Xi = \{\xi_1, \xi_2, \dots, \xi_{n+p+1}\}$ , and  $\mathcal{H} = \{\eta_1, \eta_2, \dots, \eta_{m+q+1}\}$ . A B-Spline surface and its control net are shown in Fig.3 which is evaluated using equation (4).

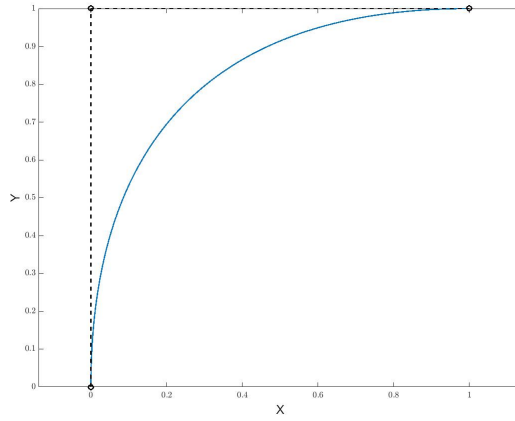


Figure 2: B-spline basis curve of order  $p = 2$  was constructed using knot vector  $\Xi = \{0, 0, 0, .5, 1, 1, 1\}$

### 2.3 Non-Uniform Rational B-Splines

The move from non-rational B-splines to Non-Uniform Rational B-splines (NURBS) was crucial because it enabled the precise representation of a broad variety of objects that cannot be properly represented by polynomials, including those that are prevalent in engineering design. To prop-

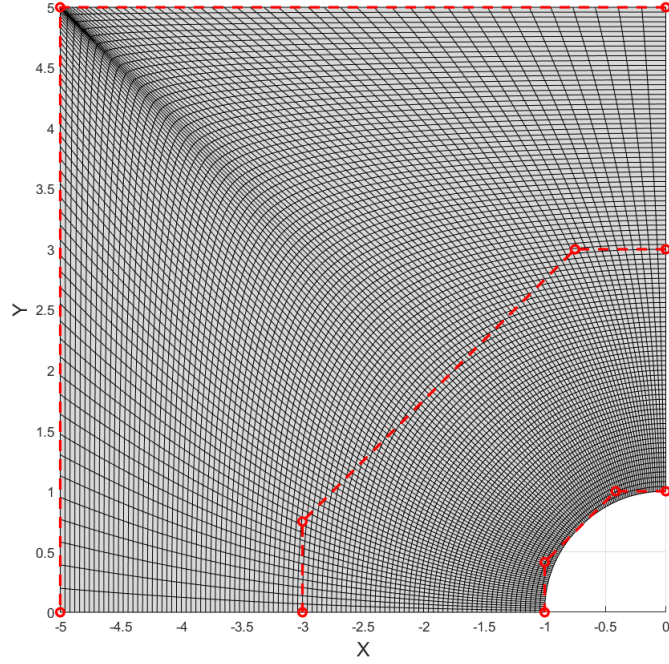


Figure 3: B-spline surface of order  $p = 2$  was constructed using the knot vectors  $\Xi_1 = \{0, 0, 0, .5, 1, 1, 1\}$  and  $\Xi_2 = \{0, 0, 0, 1, 1, 1\}$  along the first and second directions.

erly comprehend how to deal with NURBS entities, it is vital to comprehend them both geometrically and algebraically. The NURBS description can be seen as the projection of a B-Spline from a higher dimension. The control points of a curve constructed with NURBS are given as:

$$(\mathbf{B}_i)_j = (\mathbf{B}_i^w)_j / w_i, \quad j = 1, \dots, d \quad (5)$$

$$w_i = (\mathbf{B}_i^w)_{d+1}, \quad (6)$$

where  $(\mathbf{B}_i)_j$  is the  $j^{\text{th}}$  component of the vector  $\mathbf{B}_i$  and  $w_i$  is referred to as the  $i^{\text{th}}$  weight. The

NURBS is given by

$$R_i^p(\xi) = \frac{N_{i,p}(\xi)w_i}{W(\xi)} = \frac{N_{i,p}(\xi)w_i}{\sum_{i=1}^n N_{i,p}(\xi)w_i}, \quad (7)$$

and NURBS curve is given by

$$\mathbf{C}(\xi) = \sum_{i=1}^n R_i^p(\xi)\mathbf{B}_i, \quad (8)$$

while the two-dimensional NURBS basis function is calculated as

$$R_{i,j}^{p,q}(\xi, \eta) = \frac{N_{i,p}(\xi)M_{j,q}(\eta)w_{i,j}}{\sum_{i=1}^n \sum_{j=1}^m N_{i,p}(\xi)M_{j,q}(\eta)w_{i,j}} \quad (9)$$

In order to illustrate the benefit of using NURBS for the geometry, the difference between B-spline and NURBS curves are shown in Fig. 4. Note that these curves are constructed using the same control points and knot vectors. It turns out that we can produce a perfect quarter circle by changing the weight corresponding to the middle control points from 1 to  $\cos(45^\circ)$ .

## 2.4 Multi patch geometries

It is necessary to construct the computational domains using multiple NURBS patches in almost all practical situations. A multi-path domain also facilitates modeling of the multi-material domains as a different material property can be considered for each patch. Additionally, it is more convenient to perform multi-patch analyses from the perspective of data structures as it facilitates the need to split the computational domains and perform parallel computing on a machine with multiple processors. The scenario when the domain only deviates topologically from a cube is the most frequent. The tensor product nature of a patch's parameter space renders it unsuitable for modeling intricate, multiple-connected domains. By constructing the domain with multiple

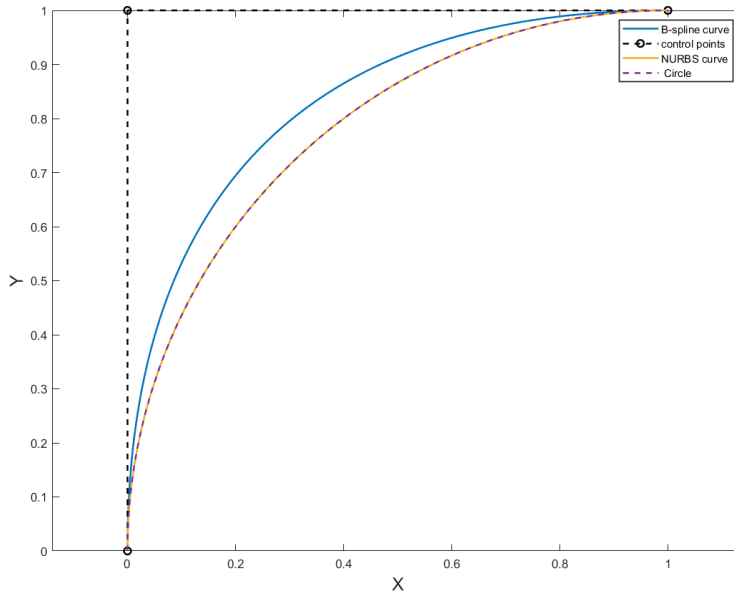
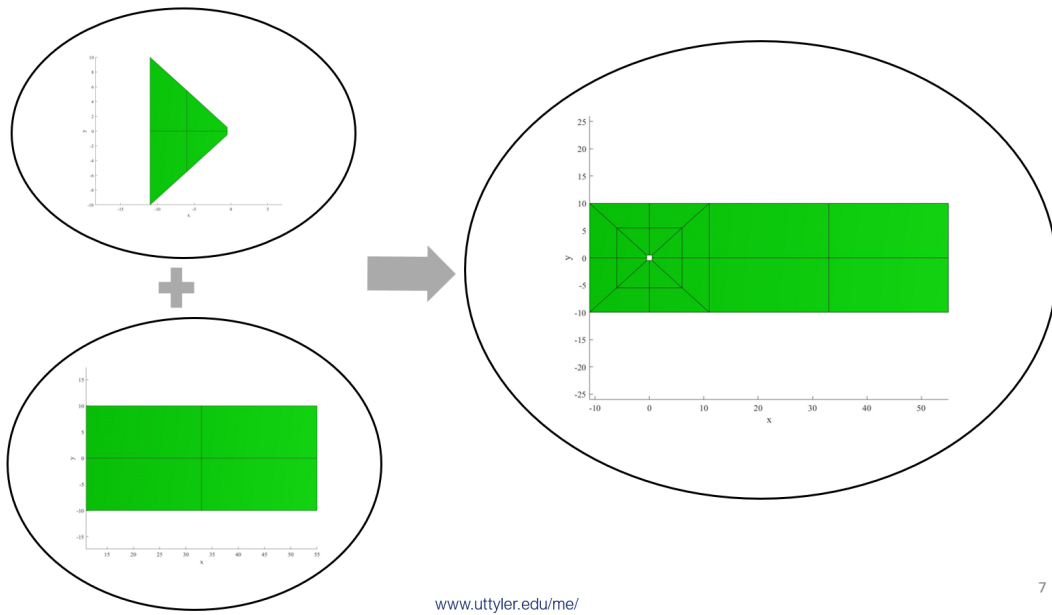


Figure 4: Difference between B-spline basis curve, NURBS curve and quarter circle constructed using same knot vector  $\Xi = \{0, 0, 0, .5, 1, 1, 1\}$

patches such geometries are generally handled easier. A computational domain made of five simple patches is shown in Fig. 5.

## 2.5 Knot insertion

Knot insertion is the simplest method of refinement and equivalent to  $h$  refinement in conventional FEA. It is possible to increase the number of elements in a computational domain by inserting additional knots without altering geometry of the domain. An example of knot insertion Fig.7, Fig.6, and Fig.8 where the number of elements increased similarly in both parametric directions.



7

Figure 5: Multi-patch geometry constructed from 5 simple patches

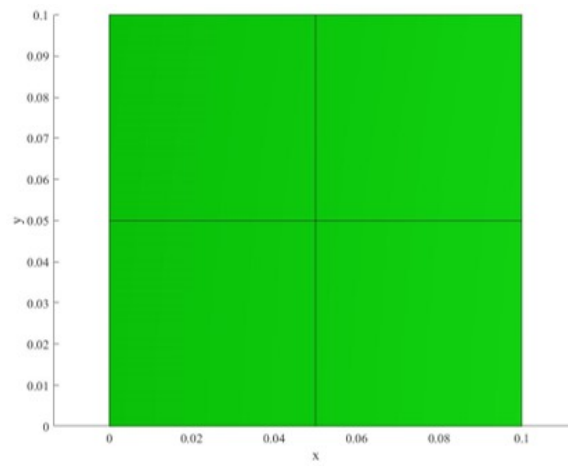


Figure 6: Square geometry represented with a coarse mesh

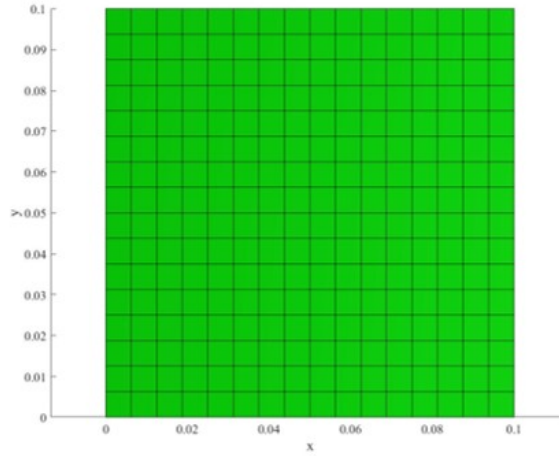


Figure 7: Square geometry after four levels of refinement

### 3 Strong and weak formulations

#### 3.1 Finite Element formulation of Navier-stokes equations

The model of viscous flow of an incompressible, unsteady Newtonian fluid can be described by the Navier-Stokes equations represented in strong form as:

$$\rho \frac{\partial \mathbf{u}}{\partial t} + \rho(\mathbf{u} \cdot \nabla \mathbf{u}) = \nabla \cdot \boldsymbol{\tau} - \nabla p,$$

$$\nabla \cdot \mathbf{u} = 0,$$

Since  $\rho$  is the density,  $\mathbf{u}$  is the velocity vector,  $p$  is the isotropic pressure and the stress tensor  $\boldsymbol{\tau}$  is given by:

$$\boldsymbol{\tau} = 2\eta \mathbf{D}$$

where  $\eta$  is the constant shear viscosity, and  $\mathbf{D}$  is the rate of the strain tensor given by:

$$\mathbf{D} = \frac{1}{2} (\nabla \mathbf{u} + (\nabla \mathbf{u})^T).$$

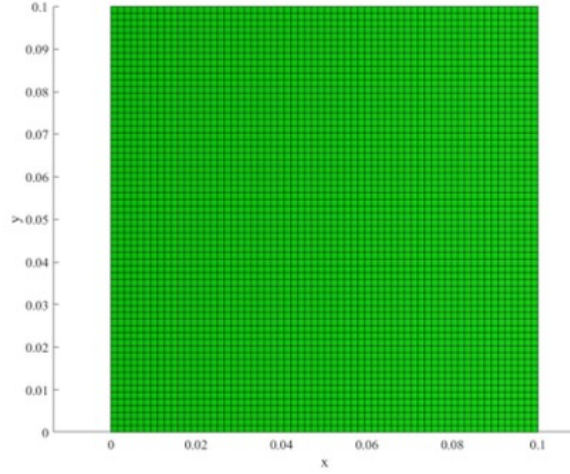


Figure 8: Square geometry after **eight** levels of refinement

From a mathematical point of view, it is preferred to use the dimensionless formulation of the governing equation as shown:

$$x^* = \frac{x}{L}, y^* = \frac{y}{L}, \mathbf{u}^* = \frac{\mathbf{u}}{u_\infty}, t^* = \frac{tu_\infty}{L}, p^* = \frac{p - p_\infty}{\rho u_\infty^2} \text{ and } \tau^* = \frac{\tau}{\rho u_\infty^2},$$

where  $L$  is a characteristic length,  $u_\infty$  is the free stream velocity and  $p_\infty$  is the free stream pressure. Omitting the asterisk (\*) for simplicity, the dimensionless Cartesian form of the governing equations can be written as:

$$\begin{aligned} \frac{\partial u}{\partial x} + \frac{\partial v}{\partial y} &= 0 \\ \frac{\partial u}{\partial t} + u \frac{\partial u}{\partial x} + v \frac{\partial u}{\partial y} &= -\frac{\partial p}{\partial x} + \frac{1}{Re} \left( \frac{\partial^2 u}{\partial x^2} + \frac{\partial^2 u}{\partial y^2} \right), \\ \frac{\partial v}{\partial t} + u \frac{\partial v}{\partial x} + v \frac{\partial v}{\partial y} &= -\frac{\partial p}{\partial y} + \frac{1}{Re} \left( \frac{\partial^2 v}{\partial x^2} + \frac{\partial^2 v}{\partial y^2} \right) \end{aligned}$$

where  $u$  and  $v$  are the horizontal and vertical velocity component respectively,  $t$  is the physical time and  $Re$  is the Reynolds number defined as:

$$Re = \frac{u_\infty L}{\nu}$$

where  $\nu$  is the kinematic viscosity.

### 3.1.1 Pressure stabilization technique

For unsteady, in-compressible fluids, the continuity equation is a constraint equation for the velocity field rather than an evolution equation for the density field. Therefore, changes in pressure are no longer affecting the density which breaks the link between the continuity and the momentum equations. stabilization technique [16, 65] is used to overcome this difficulty and to recover the link between the continuity and the momentum equations. The continuity equation has been modified and constructed by adding a Laplacian term as follows:

$$\frac{\partial u}{\partial x} + \frac{\partial v}{\partial y} = \varepsilon \nabla^2 p$$

As a result, similar order of interpolation functions can be used for pressure and velocity fields which decreases the computational cost [66]. With this formulation, the conservation equations are coupled and the pressure checker boarding can be avoided.

### 3.1.2 Modifications of the strong form

The velocity and pressure fields are defined in parameter space, while the governing equations are formulated in physical space. To evaluate the fields in physical space, the modified continuity

equation in non-dimensional form reads:

$$\begin{aligned}
\frac{\partial^2 p}{\partial x^2} + \frac{\partial^2 p}{\partial y^2} &= \frac{1}{\epsilon} \left( \frac{\partial u}{\partial x} + \frac{\partial v}{\partial y} \right); \quad \epsilon = O(\Delta t) \\
\frac{\partial u}{\partial t} + u \frac{\partial u}{\partial x} + v \frac{\partial u}{\partial y} &= -\frac{\partial p}{\partial x} + \frac{1}{\text{Re}} \left( \frac{\partial^2 u}{\partial x^2} + \frac{\partial^2 u}{\partial y^2} \right) \\
\frac{\partial v}{\partial t} + u \frac{\partial v}{\partial x} + v \frac{\partial v}{\partial y} &= -\frac{\partial p}{\partial y} + \frac{1}{\text{Re}} \left( \frac{\partial^2 v}{\partial x^2} + \frac{\partial^2 v}{\partial y^2} \right)
\end{aligned} \tag{10}$$

### 3.2 Weak formulation

In order to derive the weak formulation, we used Galerkin method. Starting with Continuity equation, we gets:

$$\begin{aligned}
\frac{1}{\epsilon} \iint N_i \left( \frac{\partial u}{\partial x} + \frac{\partial v}{\partial y} \right) dA + \left[ \iint \frac{\partial N_i}{\partial x} \frac{\partial N_j}{\partial x} + \frac{\partial N_i}{\partial y} \frac{\partial N_j}{\partial y} dA \right] p_j - \oint N_i \frac{\partial p}{\partial n} dS &= 0 \\
\left[ \iint \frac{\partial N_i}{\partial x} \frac{\partial N_j}{\partial x} + \frac{\partial N_i}{\partial y} \frac{\partial N_j}{\partial y} dA \right] p_j - \left[ \oint N_i \frac{\partial N_j}{\partial n} dS \right] p_j = -\frac{1}{\epsilon} \iint N_i \left( \frac{\partial u}{\partial x} + \frac{\partial v}{\partial y} \right) dA & \\
K_{ij} p_j = r_i^p & \tag{11}
\end{aligned}$$

$$\begin{aligned}
K_{ij} &= \iint \frac{\partial N_i}{\partial x} \frac{\partial N_j}{\partial x} + \frac{\partial N_i}{\partial y} \frac{\partial N_j}{\partial y} dA - \oint N_i \frac{\partial N_j}{\partial n} dS \\
r_i^p &= -\frac{1}{\epsilon} \iint N_i \left( \frac{\partial u}{\partial x} + \frac{\partial v}{\partial y} \right) dA
\end{aligned}$$

While the x momentum weak form states as follow :

$$\iint N_i \frac{\partial u}{\partial t} dA + \iint \left( u \frac{\partial u}{\partial x} + v \frac{\partial u}{\partial y} \right) w_i dA + \iint w_i \frac{\partial p}{\partial x} dA + \frac{1}{\text{Re}} \iint \left( \frac{\partial w_i}{\partial x} \frac{\partial u}{\partial x} + \frac{\partial w_i}{\partial y} \frac{\partial u}{\partial y} \right) dA - \oint w_i \frac{\partial u}{\partial n} dS = 0$$

$$M_{ij} w_j^{n+1} = r_i^u$$

$$M_{ij} = \iint N_i N_j dA \implies MLV = \iint N_i dA$$

$$r_i^v = MLV u_j^n - \Delta t \left[ \iint \left( u \frac{\partial u}{\partial x} + v \frac{\partial u}{\partial y} \right) w_i dA + \iint w_i \frac{\partial p}{\partial x} dA + \frac{1}{\text{Re}} \iint \left( \frac{\partial w_i}{\partial x} \frac{\partial u}{\partial x} + \frac{\partial w_i}{\partial y} \frac{\partial u}{\partial y} \right) dA \right]$$

$$r_i^{v \text{ approx}} = MLV u_j^n - \Delta t \left[ \iint \left( u \frac{\partial u}{\partial x} + v \frac{\partial u}{\partial y} \right) w_i dA + \iint N_i \frac{\partial p}{\partial x} dA + \frac{1}{\text{Re}} \iint \left( \frac{\partial N_i}{\partial x} \frac{\partial u}{\partial x} + \frac{\partial N_i}{\partial y} \frac{\partial u}{\partial y} \right) dA \right] \tag{12}$$

The y momentum equation:

$$\iint N_i \frac{\partial v}{\partial t} dA + \iint \left( u \frac{\partial v}{\partial x} + v \frac{\partial v}{\partial y} \right) w_i dA + \iint w_i \frac{\partial p}{\partial y} dA + \frac{1}{\text{Re}} \iint \left( \frac{\partial w_i}{\partial x} \frac{\partial v}{\partial x} + \frac{\partial w_i}{\partial y} \frac{\partial v}{\partial y} \right) dA - \oint w_i \frac{\partial v}{\partial n} dS = 0$$

$$M_{ij} u v_j^{n+1} = r_i^v$$

$$M_{ij} = \iint N_i N_j dA \implies MLV = \iint N_i dA$$

$$r_i^v = MLV v_j^n - \Delta t \left[ \iint \left( u \frac{\partial v}{\partial x} + v \frac{\partial v}{\partial y} \right) w_i dA + \iint w_i \frac{\partial p}{\partial y} dA + \frac{1}{\text{Re}} \iint \left( \frac{\partial w_i}{\partial x} \frac{\partial v}{\partial x} + \frac{\partial w_i}{\partial y} \frac{\partial v}{\partial y} \right) dA \right]$$

$$r_i^{v_{approx}} = MLV v_j^n - \Delta t \left[ \iint \left( u \frac{\partial v}{\partial x} + v \frac{\partial v}{\partial y} \right) w_i dA + \iint N_i \frac{\partial p}{\partial y} dA + \frac{1}{\text{Re}} \iint \left( \frac{\partial N_i}{\partial x} \frac{\partial v}{\partial x} + \frac{\partial N_i}{\partial y} \frac{\partial v}{\partial y} \right) dA \right] \quad (13)$$

### 3.3 Finite element formulation of Lighthill's acoustic analogy

In this section, the partial differential equation derived by Lighthill is solved numerically; the semi-discrete Galerkin formulation is developed first. The resulting transient formulation is then solved using the Newmark method and the harmonic solution is derived by obtaining the complex algebraic system of equation by performing Fourier transformation to the semi-discrete Galerkin nodal forces.

### 3.4 Strong and weak forms of the inhomogeneous wave equation

The governing PDE for the aeroacoustic problem by the original Lighthill's inhomogeneous wave equation is given as [22]:

$$\frac{\partial^2 \rho'}{\partial t^2} - c_0^2 \frac{\partial^2 \rho'}{\partial x_i^2} = \frac{\partial^2 T_{ij}}{\partial x_i \partial x_j}, \quad (14)$$

where  $\rho'$  representing the acoustic density fluctuation and  $T_{ij}$  is the components of the Lighthill's tensor  $[T]$  approximated as  $T_{ij} \approx \rho u_i v_j$ . To derive the weak form, the governing equation is multiplied by test functions then integrated by parts over the domain;

$$\begin{aligned}
\int_{\Omega_h} \ddot{\rho}'_h N_h d\Omega + c_0^2 \int_{\Omega_h} \nabla \rho'_h \cdot \nabla N_h d\Omega &= - \int_{\Omega_h} (\nabla \cdot T_{ij}) \cdot \nabla N_h d\Omega \\
&+ c_0^2 \int_{\Gamma_h} N_h \frac{\partial \rho'}{\partial n_i} d\Gamma \quad \forall N_h \in \vartheta_h.
\end{aligned} \tag{15}$$

The space of functions,  $\vartheta_h$ , defined as

$$\vartheta = \{ \rho'(\cdot, t) \mid \rho'(\vec{x}, t) \in H^1, \vec{x} \in \Omega \},$$

Next, we apply the finite element approximation for the density perturbation described in terms of basis function as:

$$\rho'(t) \approx \rho'_h(t) = \sum_{i=1}^{n_{\text{eq}}} N_i(\vec{x}) \rho'_i(t) \tag{16}$$

where  $N_i(\vec{x})$  denote appropriate interpolation functions. The semidiscrete Galerkin formulation can now be written in matrix form as:

$$\mathbf{M} \ddot{\rho}'(t) + \mathbf{K} \rho'(t) = f(t), \tag{17}$$

where the matrices  $\mathbf{M}$  and  $\mathbf{K}$  are computed as follows:

$$\begin{aligned}
\mathbf{M} &= [M_{ij}], \\
M_{ij} &= \int_{\Omega} N_i N_j d\Omega, & 1 \leq i, j \leq n_{\text{eq}} \\
\mathbf{K} &= [K_{ij}], \\
K_{ij} &= \int_{\Omega} c_0^2 \left( \frac{\partial N_i}{\partial x_1} \frac{\partial N_j}{\partial x_1} + \frac{\partial N_i}{\partial x_2} \frac{\partial N_j}{\partial x_2} \right) d\Omega, & 1 \leq i, j \leq n_{\text{eq}}
\end{aligned} \tag{18}$$

the right-hand-side vector including the acoustic sources reads:

$$f = \{f_i\} \quad (19)$$

$$f_i = - \int_{\Omega} \left( \frac{\partial N_i}{\partial x_1}, \frac{\partial N_i}{\partial x_2} \right) \cdot \frac{\partial T_{ij}}{\partial x_j} d\Omega + \int_{\Gamma} c_0^2 N_i \frac{\partial \rho'}{\partial n_i} d\Gamma, \quad 1 \leq i \leq n_{eq}$$

and the divergence of Lighthill's tensor can be calculated as proposed in [67] as follows:

$$\nabla \cdot T_{ij} = \rho \begin{pmatrix} 2u_1 \frac{\partial u_1}{\partial x_1} + u_2 \frac{\partial u_1}{\partial x_2} + u_1 \frac{\partial u_2}{\partial x_2} \\ u_2 \frac{\partial u_1}{\partial x_1} + u_1 \frac{\partial u_2}{\partial x_1} + 2u_2 \frac{\partial u_2}{\partial x_2} \end{pmatrix}. \quad (20)$$

Now, by using the discrete nodal values  $u_i^{(n)}$  of  $\vec{u}$ , the finite element evaluation for the terms of

the first vector component is given by:

$$2u_1 \frac{\partial u_1}{\partial x_1} = 2 \left( \sum_{n=1}^{n_{en}} N_n(\vec{x}) u_1^{(n)} \right) \left( \sum_{n=1}^{n_{en}} \frac{\partial N_n(\vec{x})}{\partial x_1} u_1^{(n)} \right),$$

$$u_2 \frac{\partial u_1}{\partial x_2} = \left( \sum_{n=1}^{n_{en}} N_n(\vec{x}) u_2^{(n)} \right) \left( \sum_{n=1}^{n_{en}} \frac{\partial N_n(\vec{x})}{\partial x_2} u_1^{(n)} \right),$$

$$u_1 \frac{\partial u_2}{\partial x_2} = \left( \sum_{n=1}^{n_{en}} N_n(\vec{x}) u_1^{(n)} \right) \left( \sum_{n=1}^{n_{en}} \frac{\partial N_n(\vec{x})}{\partial x_2} u_2^{(n)} \right),$$

where  $n_{en}$  corresponds to the number of degree of freedom per element. We can evaluate the other components of the divergence of Lighthill's tensor at each time step for the two -dimensional cases considered. The resulting vector can now be multiplied by the gradient of the basis function by numerical integration. It is then possible to obtain the acoustic source value for the right hand side at each degree of freedom.

### 3.4.1 Simulation of unbounded domains

A first order approximation of an ABC for solving the wave equation was considered in this study which resulted in a straightforward implementation in IGA similar to the ABC considered in [67]:

$$\left( c_0 \frac{\partial}{\partial x_1} - \frac{\partial}{\partial t} \right) \rho' \Big|_{x_1=0} = 0. \quad (21)$$

recalling the weak formulation of the problem 22, initially we assumed homogeneous Neumann boundary conditions which results in natural cancellation of the Neumann boundary integration. By knowing that Neumann integral applied at the boundary and equation 21 representing that changing in pressure fluctuation in the outgoing direction is equal to the change in time, it can be easily substitute 21 in equation 22 yielding to equation :

$$\int_{\Omega} \ddot{\rho}' w d\Omega + c_0^2 \int_{\Omega} \nabla \rho' \cdot \nabla w d\Omega = - \int_{\Omega} (\nabla \cdot T_{ij}) \cdot \nabla w d\Omega - c_0 \int_{\Gamma} w \frac{\partial \rho'}{\partial t} d\Gamma \quad (22)$$

The new equation now has new surface integral including changing in time domain that leads to a new matrix applied only on the boundary, which is called damping matrix  $\mathbf{C}$ . Hence, the semi discrete Galerking formulation changes to

$$\mathbf{M} \ddot{\rho}'(t) + \mathbf{C} \dot{\rho}'(t) + \mathbf{K} \rho'(t) = f(t), \quad (23)$$

and the damping matrix is calculated as :

$$\mathbf{C} = [C_{ij}], \quad C_{ij} = c_0 \int_{\Gamma} N_i N_j d\Gamma. \quad (24)$$

### 3.4.2 Time discretization

Newmark scheme[68] usually used for hyperbolic partial differential equations, so we have:

$$\begin{aligned}\underline{\rho}'_{n+1} &= \underline{\rho}'_n + \Delta t \underline{\dot{\rho}}'_n + \frac{\Delta t^2}{2} \left( (1 - 2\beta_H) \underline{\ddot{\rho}}'_n + 2\beta_H \underline{\ddot{\rho}}'_{n+1} \right) \\ \underline{\dot{\rho}}'_{n+1} &= \underline{\dot{\rho}}'_n + \Delta t \left( (1 - \gamma_H) \underline{\ddot{\rho}}'_n + \gamma_H \underline{\ddot{\rho}}'_{n+1} \right).\end{aligned}$$

applying in equation

$$\mathbf{M}\ddot{\rho}'(t) + \mathbf{C}\dot{\rho}'(t) + \mathbf{K}\rho'(t) = f(t), \quad (25)$$

now we can write the solution of the predictor-corrector algorithm as an Effective stiffness formulation [69] as follows :

Effective Stiffness Formulation - Perform predictor step:

$$\begin{aligned}\underline{\tilde{\rho}}' &= \underline{\rho}'_n + \Delta t \underline{\dot{\rho}}'_n + (1 - 2\beta_H) \frac{\Delta t^2}{2} \underline{\ddot{\rho}}'_n \\ \underline{\tilde{\dot{\rho}}}' &= \underline{\dot{\rho}}'_n + \Delta t (1 - \gamma_H) \underline{\ddot{\rho}}'_n\end{aligned} \quad (26)$$

- Solve algebraic system of equations:

$$\begin{aligned}\mathbf{K}^* \underline{\rho}'_{n+1} &= \underline{f}_{n+1} - \mathbf{C} \underline{\tilde{\dot{\rho}}}' + \left( \frac{1}{\beta_H \Delta t^2} \mathbf{M} + \frac{\gamma_H}{\beta_H \Delta t} \mathbf{C} \right) \underline{\tilde{\rho}}' \\ \mathbf{K}^* &= \mathbf{K} + \frac{\gamma_H}{\beta_H \Delta t} \mathbf{C} + \frac{1}{\beta \Delta t^2} \mathbf{M}\end{aligned} \quad (27)$$

- Perform corrector step:

$$\begin{aligned}\underline{\ddot{\rho}}' &= \frac{\underline{\rho}'_{n+1} - \underline{\tilde{\rho}}'}{\beta \Delta t^2} \\ \underline{\dot{\rho}}'_{n+1} &= \underline{\dot{\rho}}'_n + \gamma_H \Delta t \underline{\ddot{\rho}}'\end{aligned} \quad (28)$$

### 3.5 Harmonic formulation

In order to obtain the harmonic solution, a Fourier transformation was applied to the semi-discrete Galerkin equations at the degrees of freedom [67], so it becomes possible to compute the sound ra-

diation for specific frequency components present in acoustic sources [70], which led to the equation (29):

$$(-\omega^2\mathbf{M} - i\omega\mathbf{C} + \mathbf{K}) \underline{\hat{\rho}} = \underline{\hat{f}}, \quad (29)$$

where  $\hat{f}$  is the complex acoustic source, obtained from the Fourier transform,  $\mathbf{K}$ ,  $\mathbf{M}$  and  $\mathbf{C}$  are the stiffness, mass, and damping matrix respectively. Although time-consuming calculations are required to transform the transient data, considerable saving is achieved by performing time-harmonic wave propagation analyses. Computations are performed for the targeted frequency which avoids the transfer of numerical noise from transient results. Time harmonic analyses also will make it feasible to target a specific frequency with the maximum amplitude using noise reduction MMs specifically designed for the targeted frequency in order to eliminate or minimize the noise generated due to airflow. This will be demonstrated later in Section 5.3.

## 4 Validation

### 4.1 ABC for wave equation

In this section, the first-order absorbing boundary condition is tested against a sinusoidal simple pulse in a square domain, calculations are carried out for both absorbing and Neumann boundary conditions and compared to each other. As a case study as a sinusoidal signal with frequency  $f = 10\text{kHz}$  applied at the center of a  $L \times L = 100 \text{ mm} \times 100 \text{ mm}$  square where the center coincides with the origin and the acoustic pressure distribution is shown in Fig. 10. Fixing the speed of sound as  $c_0 = 343 \text{ m/s}$  in air, the wave-length was  $\lambda = 34.3 \text{ mm}$ . The total computation time was discretized using a time step of  $\Delta t = 2.5\mu \text{ s}$  corresponding to a discretization ratio of 40-time

steps per period. Second order Bernstein basis function was used for space discretization, similar parameters have been used in [67], and the numerical results matched those presented in this reference. The total number of elements was 2401 corresponding to 2601 degrees of freedom. The mesh used is shown in Fig.9.

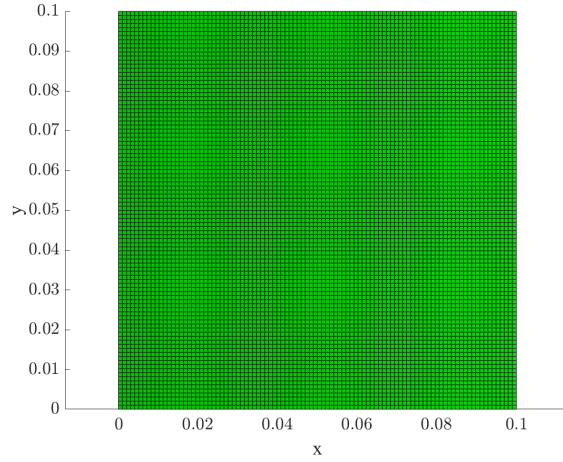


Figure 9: Mesh for the proposed space with 2401 total number of elements.

Instead of imposing ABC an implicit homogeneous Neumann boundary conditions was imposed on the outer boundary of the domain. A small error is noticeable when comparing the solution are shown in Fig. 12 with the one obtained with ABC and plotted in Fig. 11. This is because the wave did not fully reach the outer boundary. Instead to simulating an infinite domain a full reflection happened when homogeneous Neumann boundary conditions was imposed as seen in Fig. 14, and Fig. 16 which led to incorrect estimation of the pressure fluctuation. After reaching  $t = 195\mu[s]$ , the reflected wave has already dominated the solution, and the computation had no physical meaning. The effective reflection rate was  $R = 1$  which means this types of boundary condition acts as solid walls. On the contrary, the results from applying first order absorbing

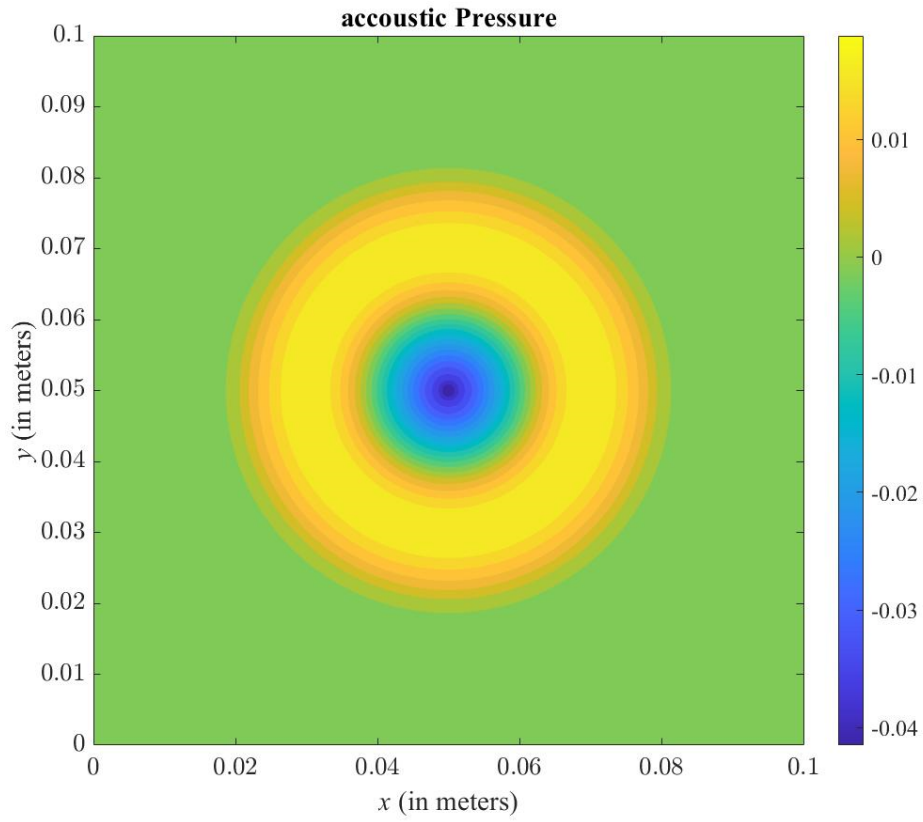


Figure 10: The acoustic pressure distribution due to a sinusoidal signal with frequency  $f = 10\text{kHz}$  applied at the center of a rectangular domain

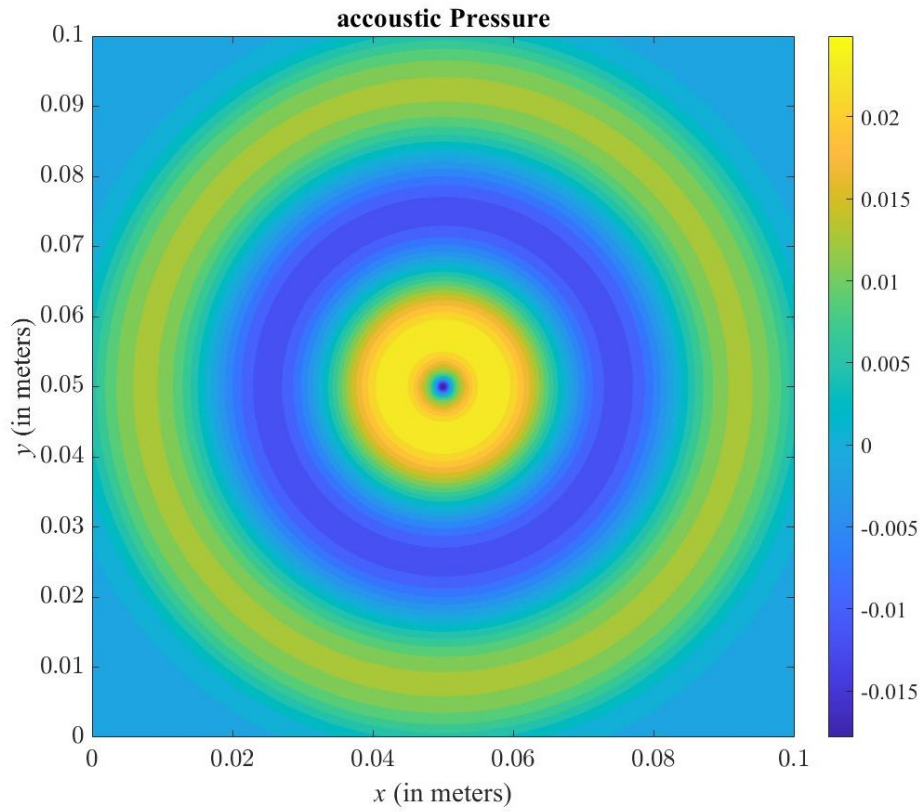


Figure 11: Pressure distribution at  $t = 1.65E - 4$  s with ABC.

boundary condition showing good absorbing properties before and after the wave hits the outer boundary. There is no visible reflection in Fig. 11 when the waves reaches the end of computational domain. The wave travels out from the boundary as it is not there. This behaviour did not change with time as shown in Fig. 13 and Fig. 15 and the wave travels out of computational domain mimicking infinite space.

Finally, the variation of pressure distribution with time is shown in Fig. 17 for a fixed point in the square domain located at  $(x_1, x_2) = (50 \text{ mm}, 25 \text{ mm})$  for both both Neumann boundary condition

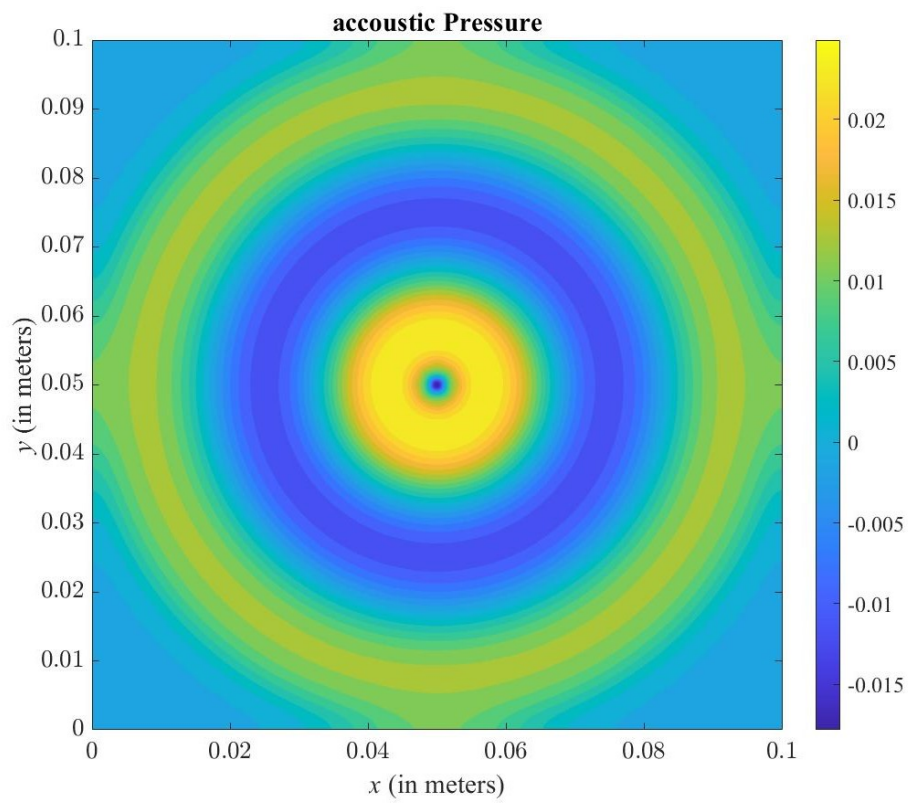


Figure 12: Pressure distribution at  $t = 1.65E - 4$  s without ABC.

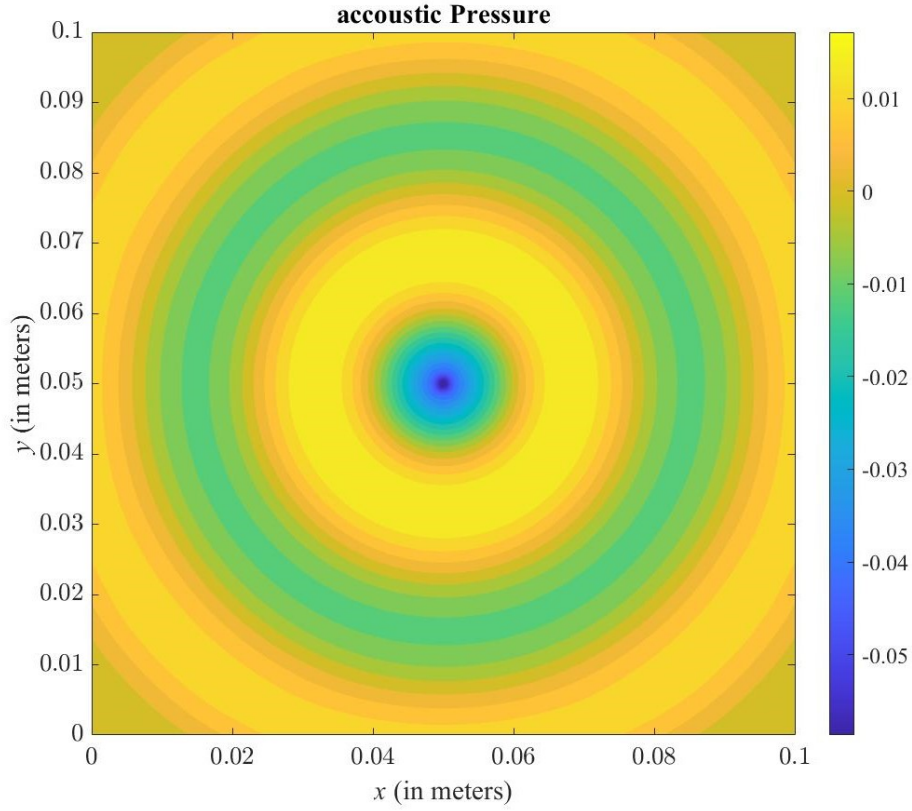


Figure 13: Pressure distribution at  $t = 1.95E - 4$  s with ABC.

and ABC. When imposing homogeneous Neumann boundary conditions, the non-physical reflected wave directly affects the incoming wave producing a total wave about double the amplitude of correct solution. As for the Absorbing boundary, no reflection can be observed for the entire computational time.

## 4.2 Lighthill's acoustic analogy

The goal of this section is to validate the implementation of lighthill's acoustic analogy in this study which solves the weak form presented in equation (22). A flow field created by the co-rotating

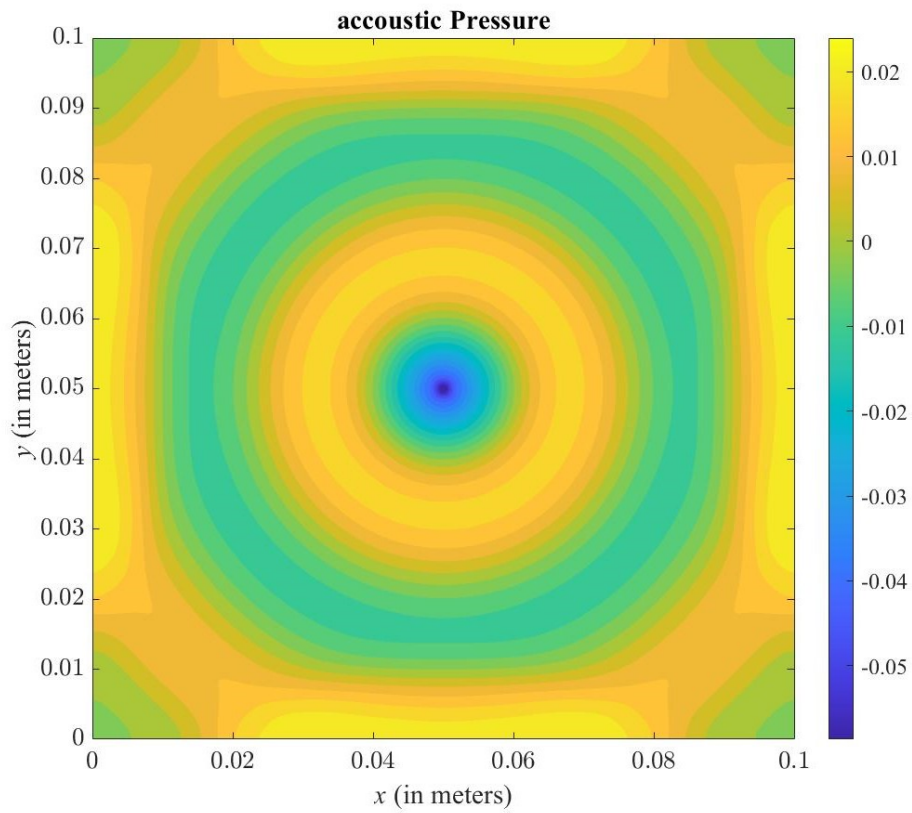


Figure 14: Pressure distribution at  $t = 1.95E - 4$  s without ABC.

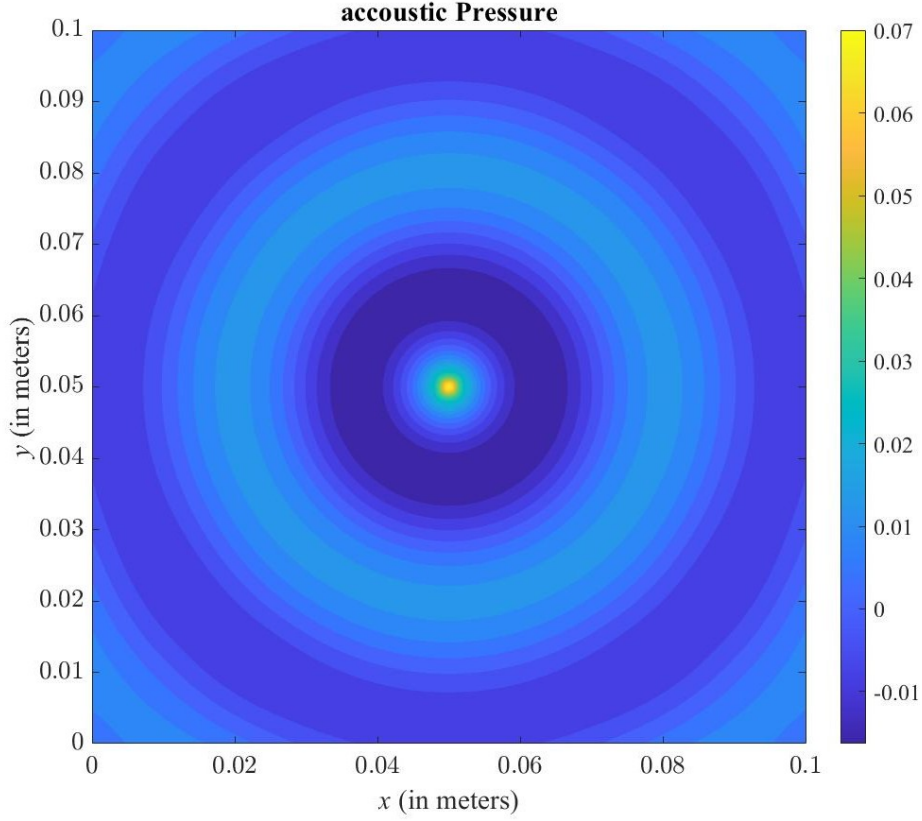


Figure 15: Pressure distribution at  $t = 2.3E - 4$  s with ABC.

vortex pairs was considered to analyze and validate a hybrid technique utilized in this study. The original Lighthill acoustic analogy [23] was implemented and the auditory sources were identified using the hydrodynamic velocity field. In the numerical examples presented in this section, the flow field generated by the spinning vortex pair was estimated using a numerical region of size  $10 \times 10$  m in which the acoustic nodal sources and acoustic propagation of the inhomogeneous wave equation were determined. In order to assess the fields, the rotating radius was set to  $r_o = .5m$ , the circulation intensity to  $= 12.00531m^2/s$ , and the sound speed to  $c_o = 1m/s$ .

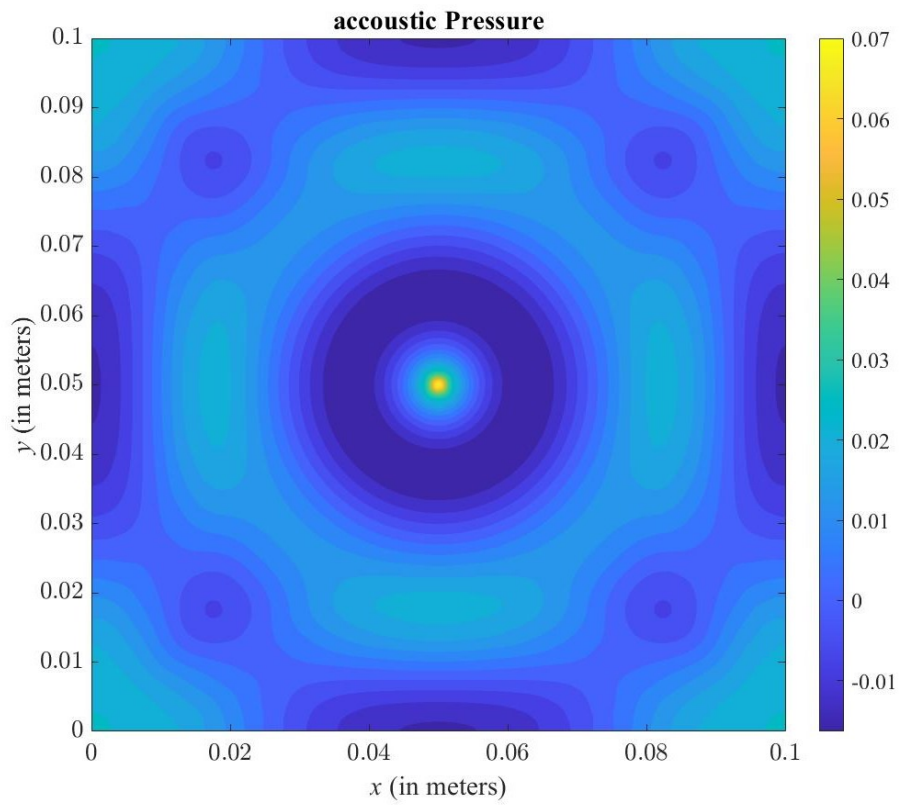


Figure 16: Pressure distribution at  $t = 2.3E - 4$  s without ABC.

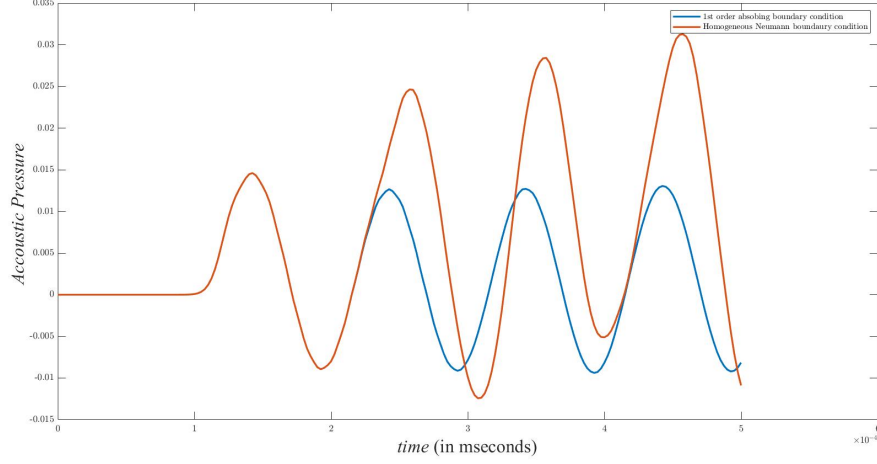


Figure 17: Evaluation of the acoustic pressure using homogeneous Neumann and first order ABC, for a point located at  $(x_1, x_2) = (50 \text{ mm}, 25 \text{ mm})$ .

Hence, the wavelength was  $1.644 \text{ m}$ . This is similar to the previous studies conducted by other authors [67, 71, 72] to validate aeroacoustics simulation platforms developed using other numerical techniques. To obtain the tangential velocity field, it is necessary to apply the vortex core model as suggested in [73–75]. At each point vortex for radii, a desingularized kernel based on the Scully model [76, 77] was applied. The equations for the velocity components are given as:

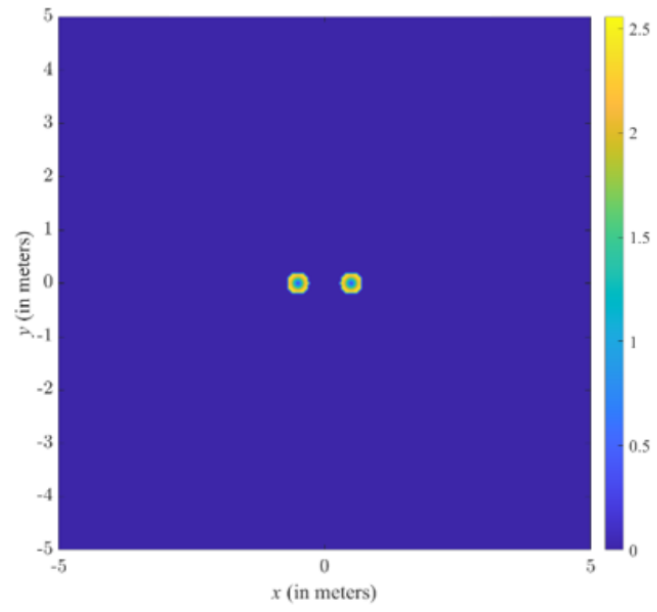
$$u_x = -\frac{\Gamma}{2\pi} \frac{y}{r_{\text{core}} + x + y^2}; u_y = \frac{\Gamma}{2\pi} \frac{x}{r_{\text{core}} + x^2 + y^2}, \quad (30)$$

The exact solution of this problem is known [78]:

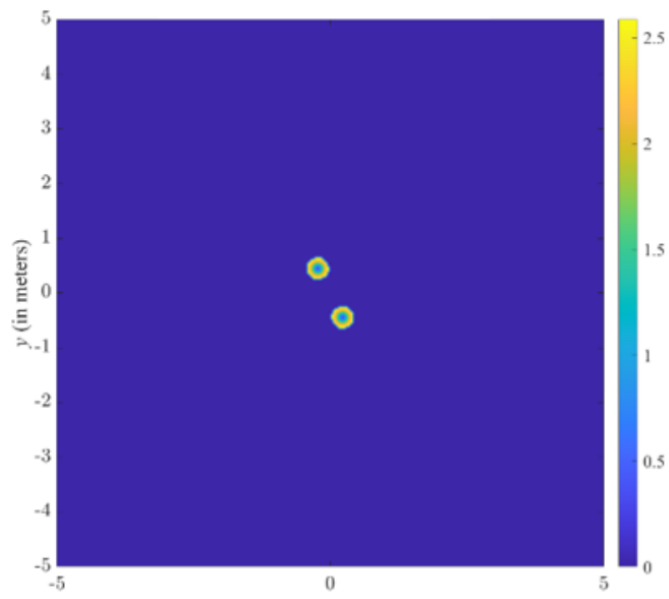
$$p' = \frac{\rho_0 \Gamma^4}{64\pi^3 r_0^4 c_0^2} [J_2(kr) \cos(\Psi) - Y_2(kr) \sin(\Psi)], \quad (31)$$

where  $Y_2(kr)$  and  $J_2(kr)$  are second order Bessel functions  $k = 2\omega$ ,  $\Psi = 2(\omega t - \theta)$  and  $p'$  is acoustic pressure.

A direct implantation of the equation(30) with  $r_o = 0.5 m$  was considered and the evolution of the velocity field with time are shown in Fig.18a and Fig. 18b. Furthermore, the corresponding forces computed as the solution of the discrete equation(19) are shown in Fig. 19a, and Fig.19b.



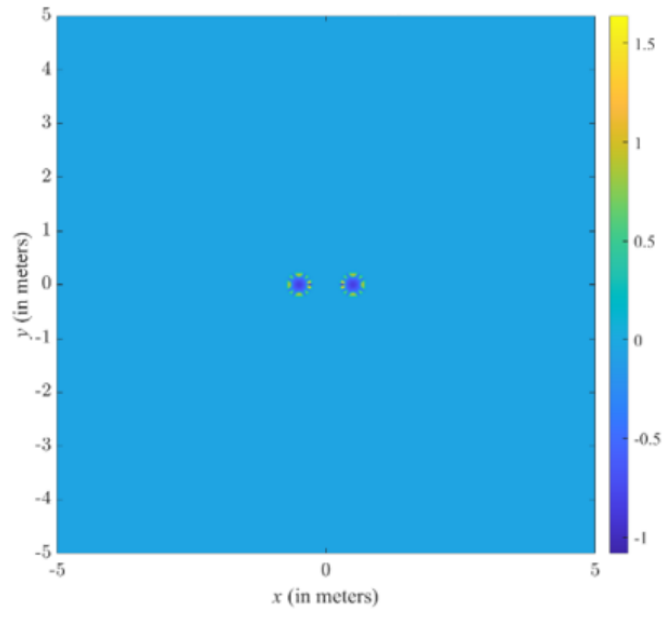
(a) time = 0s



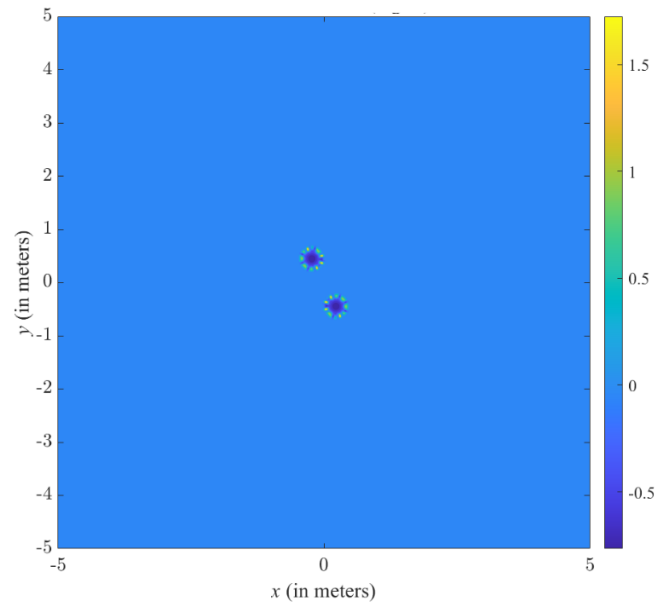
(b) time = 3s

Figure 18: Velocity field for two co-spinning vortex

Next, the acoustic pressure is solved for using the transient discrete equation (25), and plotted in Fig. 20a, Fig. 20b, Fig. 21a, and Fig. 21b and show the the acoustic pressure as it evolves with time. The spiral behavior is detected and no artificial reflection is visible from the boundary confirming the effectiveness of the ABC used.

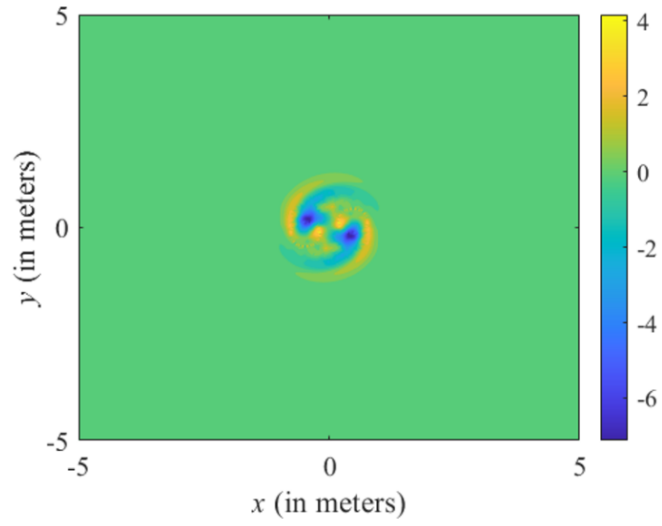


(a) time =0s

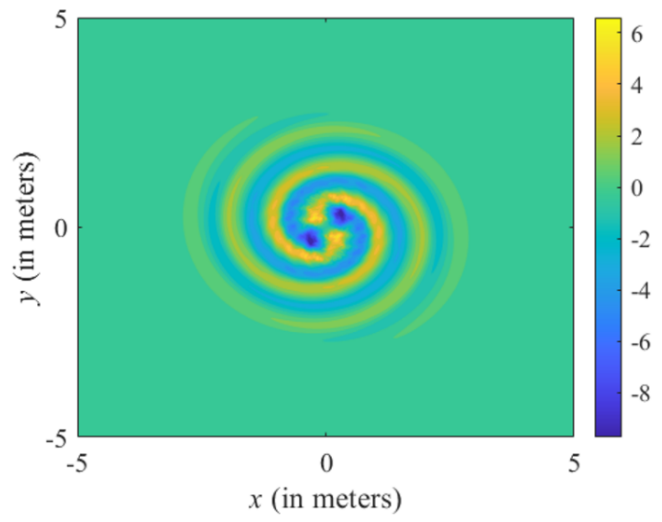


(b) time =3s

Figure 19: Acoustic sources field for two co-spinning vortex



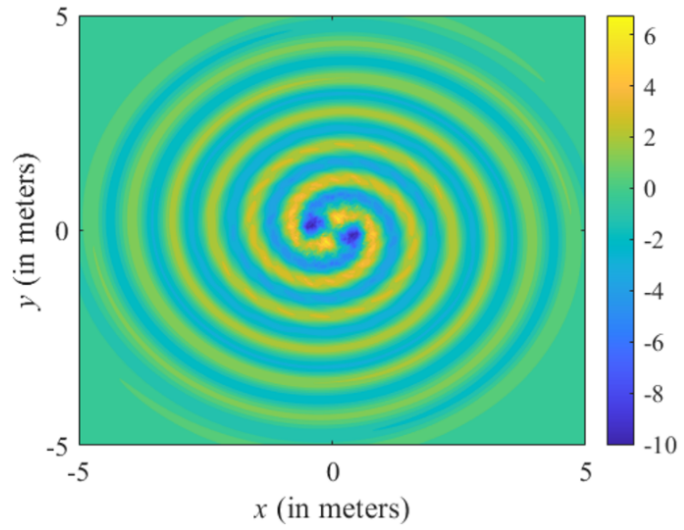
(a) time =1s



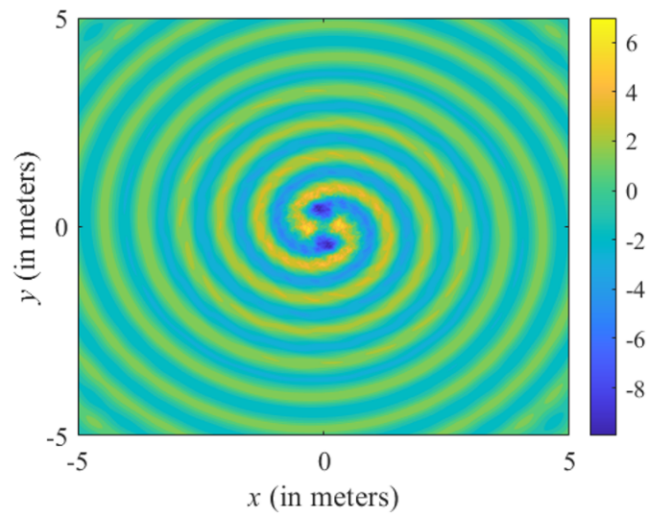
(b) time =3s

Figure 20: Acoustic pressure field ( $Pa/m$ ) for the two co-spinning vortex for different times

Please note the presence of noise in the solution of the time-dependant wave equation as shown in Fig. 21b. In contrary when solving the time-harmonic problem equation 29 shown in Fig. 22a no numerical noise is detectable while the computational time is reduced dramatically. The solution of the time-harmonic problem matches with the analytical solution shown in Fig. 22b very well which is calculated for time greater than 12s to ensure the time harmonic solution is obtained.



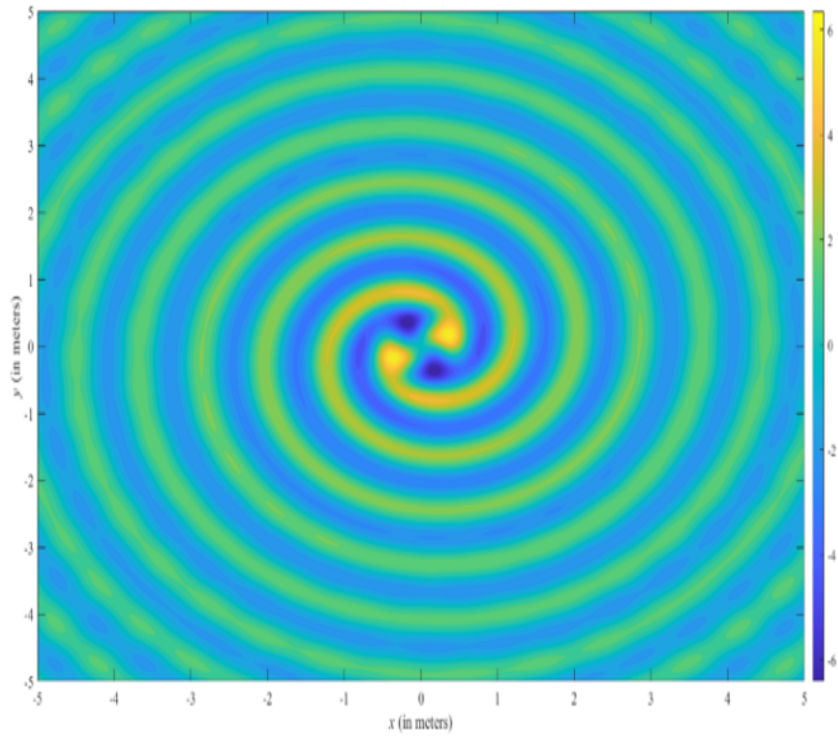
(a) time =6s



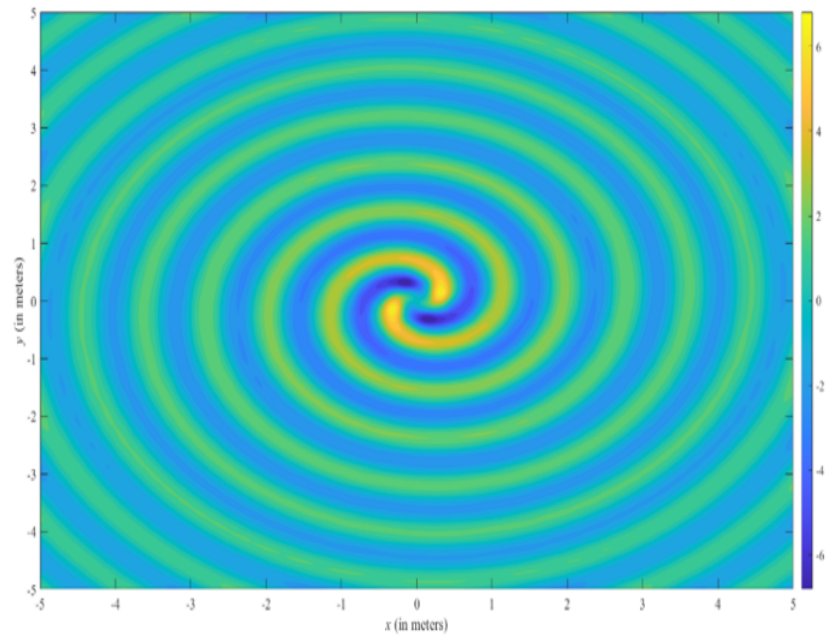
(b) time =9s

Figure 21: Acoustic pressure  $pa$  field for The two co-spinning vortex case

Finally, in order to fully able to compare the analytical and numerical solutions, the decay of the acoustic pressure is plotted along the  $x$ -axis for both numerical and analytical solutions in Fig23. A good agreement is observed corresponding to an error less than 5%. The phase shift error observed could be due to the discrete evaluation of the sources since the approximate values for velocities were calculated to avoid singularity at the center of the vortex. Also, it is noted that the acoustic source is decaying by a rate of about 10% along the  $x$ -axis as expected.



(a) Lighthill's harmonic solution for the two co-spinning vortex case



(b) Analytical harmonic solution for the two co-spinning vortex case

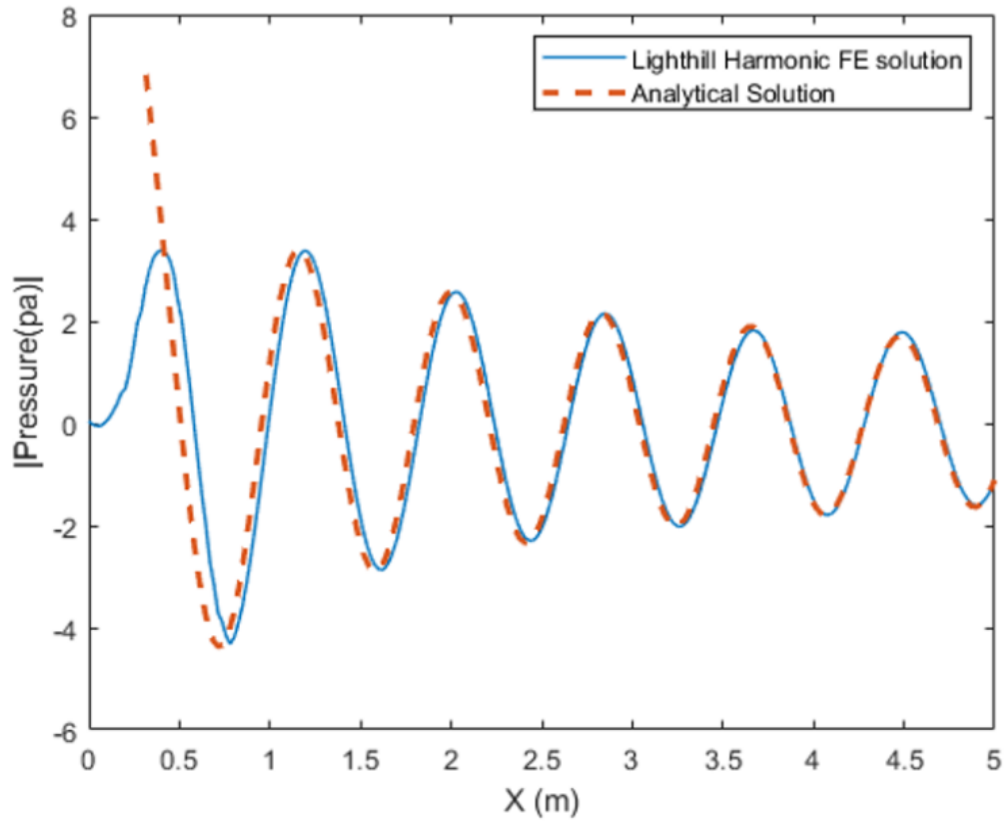


Figure 23: The decay of the acoustic pressure along the x-axis

### 4.3 Solution to Navier-Stocks equations

In order to validate the implementation of the Navier -Stocks equations, the proposed formulation was used to solve the benchmark problem of Lid-driven cavity flow. The governing equations were solved for different values of the Reynolds number and the results were compared with published studies conducted using FEA [79].

### 4.3.1 Lid-driven cavity flow

In this section, the standard benchmark the problem, lid-driven cavity flow, is introduced and solved for unsteady, incompressible fluid flow simulation. We assumed the initial boundary conditions at solid walls as a no-slip boundary condition for velocity components. Pressure is considered to be zero at the lower left corner point as shown in Fig 24, with zero gradients over the walls. The Reynolds number is changed based on the side length of the cavity and the speed of the lid.

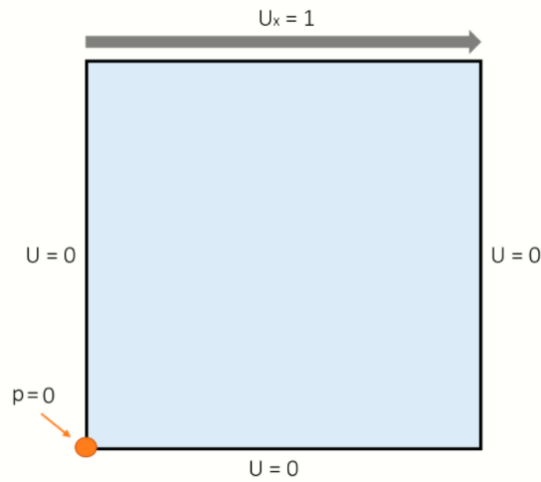


Figure 24: The boundary conditions for the lid-driven cavity model.

In this thesis, the benefits of using IGA and the possibility of reducing the computational cost were investigated. As shown in Fig. 25 a steady state velocity magnitude solution for  $Re = 100$  was found using only  $8 \times 8$  element, and the axial velocity found was validated against the results presented by G.Hirsch [80, 81] as well as those obtained using conventional FEA [79]. As illustrated in Fig. 26 the IGA solution found with only  $8 \times 8$  elements in less than two minutes matches

very well with those obtained in previous studies. In particular, conventional FEA results were found using a  $50 \times 50$  mesh grid. The reduction in the number of degrees of freedom required demonstrates the effectiveness of the proposed IGA platform for aeroacoustic analyses.

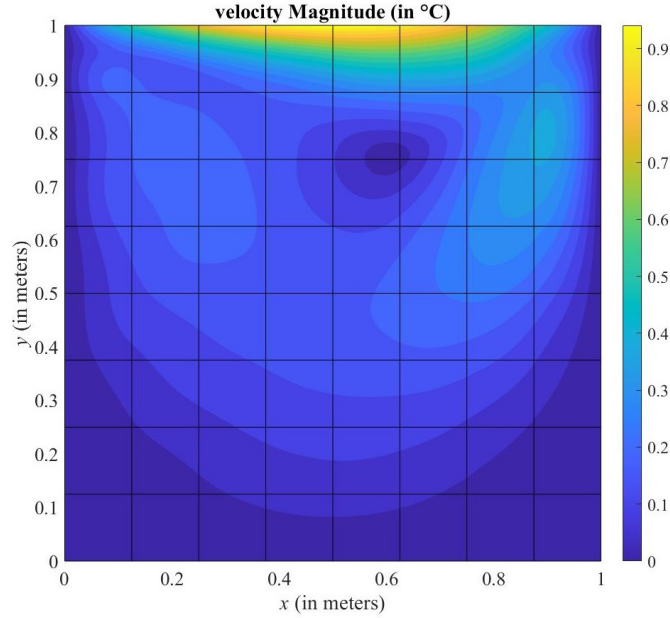


Figure 25: Velocity field for Reynolds number 100 obtained only with  $8 \times 8$  elements.

More examples, with a higher level of refinement, were obtained for this problem at a wide range of the Reynolds number values,  $Re$ , to show the effect of the Reynolds number on the primary vortex location and axial and normal velocities. The velocity and pressure fields has been plotted for  $Re = 5$  in Fig. 27a and Fig. 27b respectively. Next, the solution was found for the Reynolds numbers  $Re = 100$  and  $Re = 1000$ , and the pressure fields are shown in Fig. 28a and Fig. 29a respectively. The corresponding velocity fields are shown in Fig. 28b and Fig. 29b. In order to test the limits of the codes, the  $Re = 10,000$  has been applied to the cavity problem. Surprisingly reliable results were found as shown in Fig. 30a and Fig. 30b. The pressure stabilization factor was

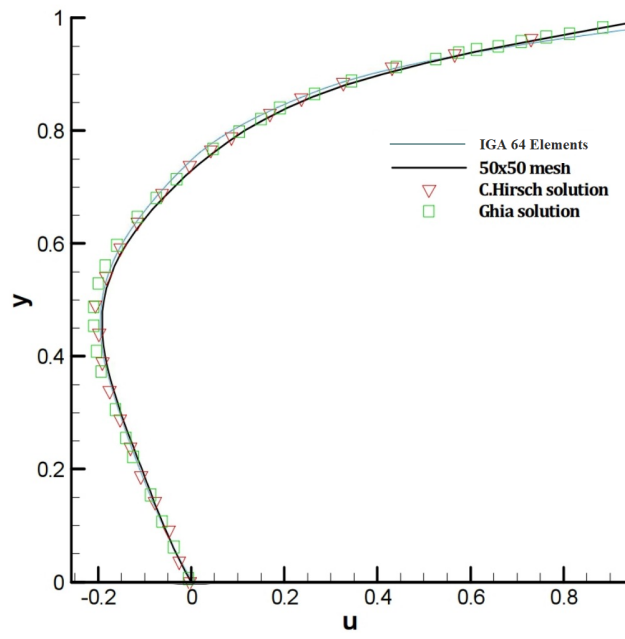
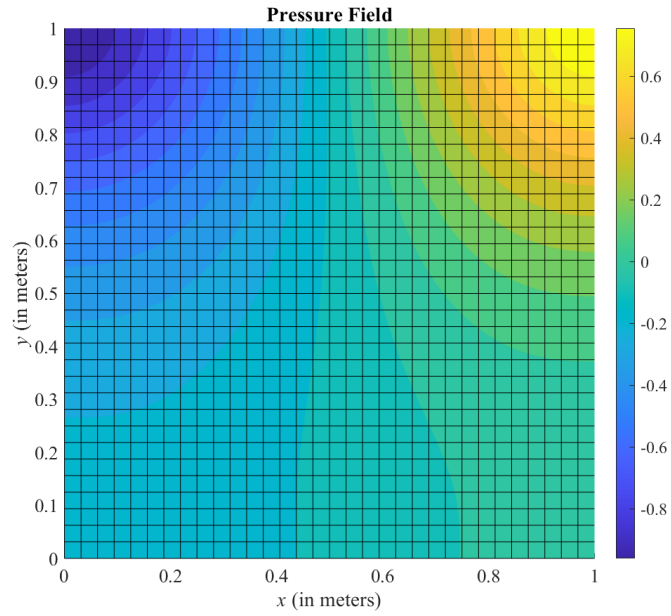
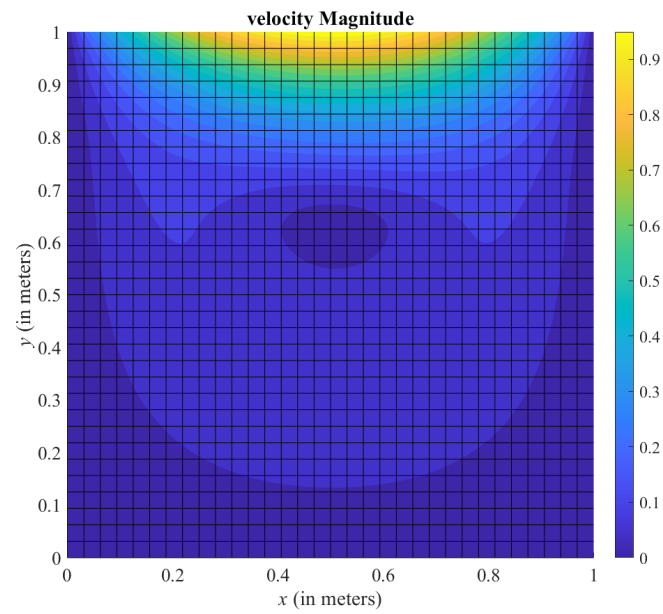


Figure 26: Axial velocity for different solutions against IGA using only  $8 \times 8$  elements .

taken to be 0.01 with a time step of 0.08 s for Reynolds numbers 100, 1,000, and 10,000, and a stabilization factor of 0.1 with a time step of 0.008 s was considered for  $Re = 5$ .

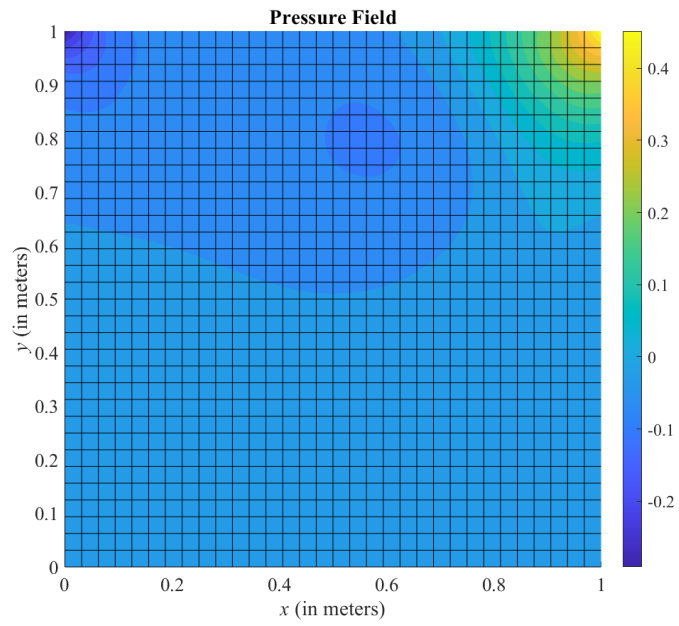


(a) Pressure field for Reynolds number  $Re = 5$  with 256 elements.



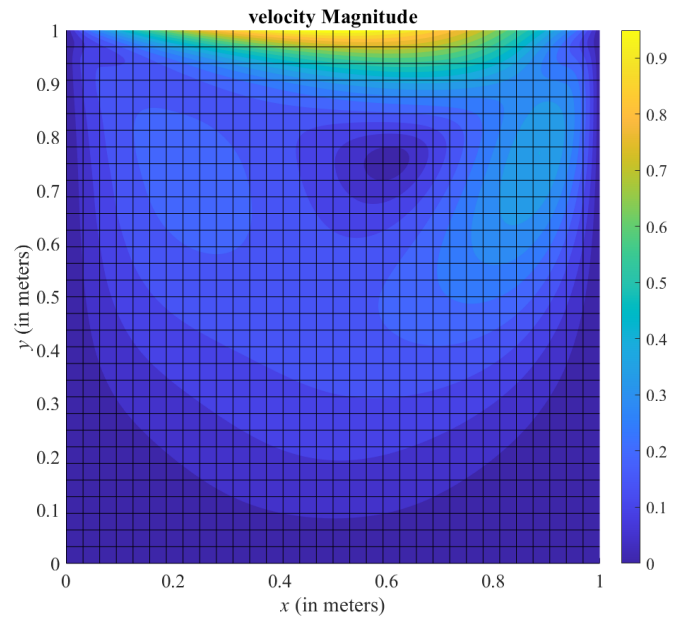
(b) Velocity field for Reynolds number  $Re = 5$  with 256 elements .

Figure 27: Velocity and pressure fields for Reynolds number  $Re = 5$ .



(a) Pressure field for Reynolds number  $Re = 100$

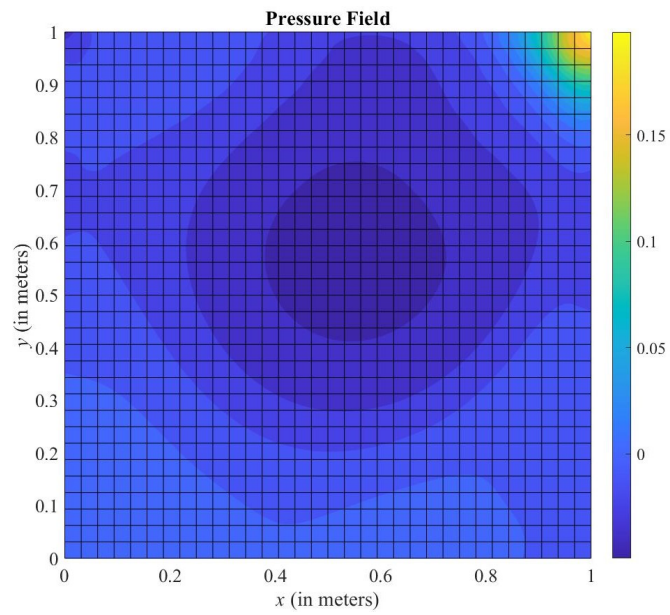
with 256 elements.



(b) Velocity field for Reynolds number  $Re = 100$

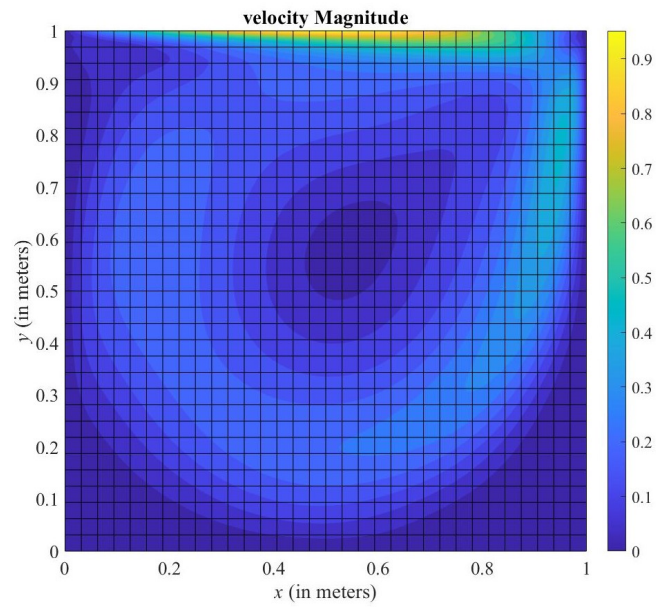
with 256 elements .

Figure 28: Velocity and pressure fields for Reynolds number  $Re = 100$ .



(a) Pressure field for Reynolds number  $Re = 1000$

with 256 elements.



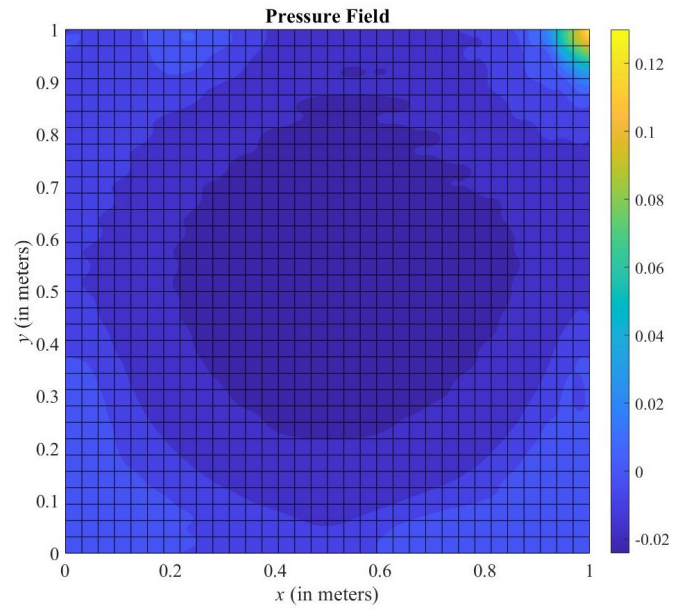
(b) Velocity field for Reynolds number  $Re = 1000$

with 256 elements.

Figure 29: Velocity and pressure fields for Reynolds  $Re = 1000$ .

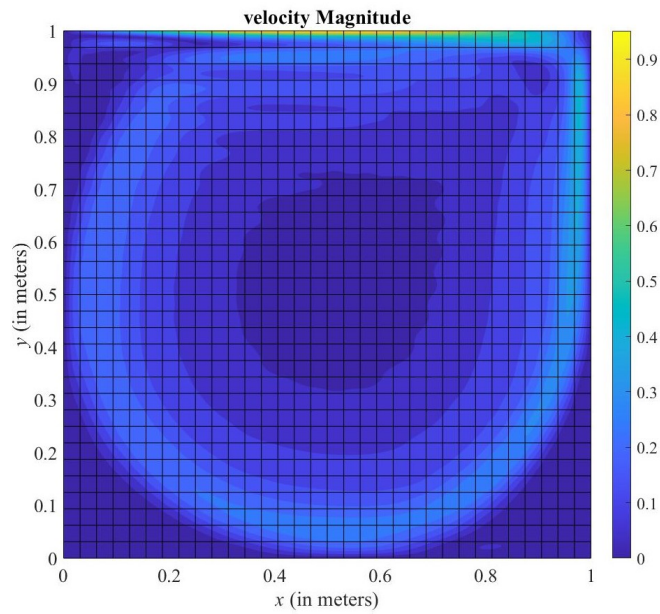
The velocity fields were validated against published results available in the literature for Reynolds numbers 100 and 1000 and the solutions presented in Fig. 28b, Fig. 31, Fig. 29b and Fig. 32 had a great match with the published results [79]. Furthermore, a very good resemblance exists for the solutions presented in Fig. 30b, Fig. 33, and those obtained using commercial CFD software.

It is interesting to note that in all the cases studied the maximum pressure field was consistently located at the right corner of the lid, which is in the direction of lid cover velocity. Also, the diameter of the vertices increased with increasing the Reynolds number, as well as the negative pressure area.



(a) Pressure field for Reynolds number  $Re = 10,000$

with 256 elements.



(b) Velocity field for Reynolds number  $Re = 10,000$

with 256 elements.

Figure 30: Velocity and pressure <sup>59</sup>fields for Reynolds  $Re = 10,000$ .

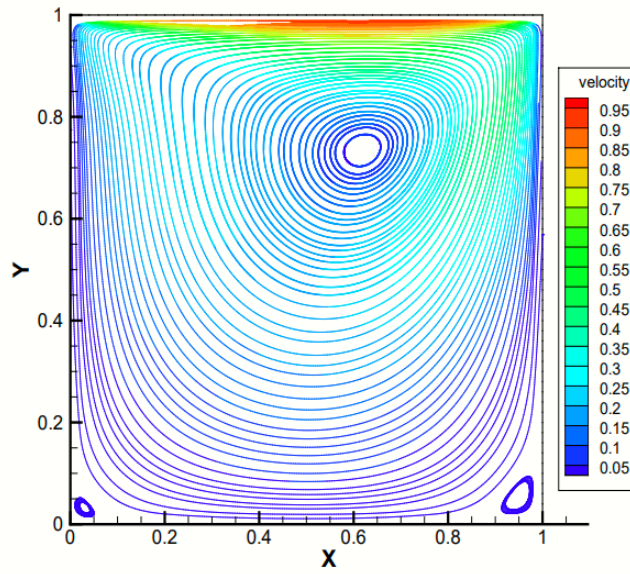


Figure 31: FEA element analysis solution for Reynolds number  $Re = 100$ .

The effect of Reynolds number can be also clearly seen from the axial and normal velocity components profiles at  $x = 0.5$  and  $y = 0.5$  as shown in Fig. 34 and Fig. 35, respectively. It can be seen that increasing the Reynolds number increases the maximum axial and normal velocity near the top of the lid-cavity.

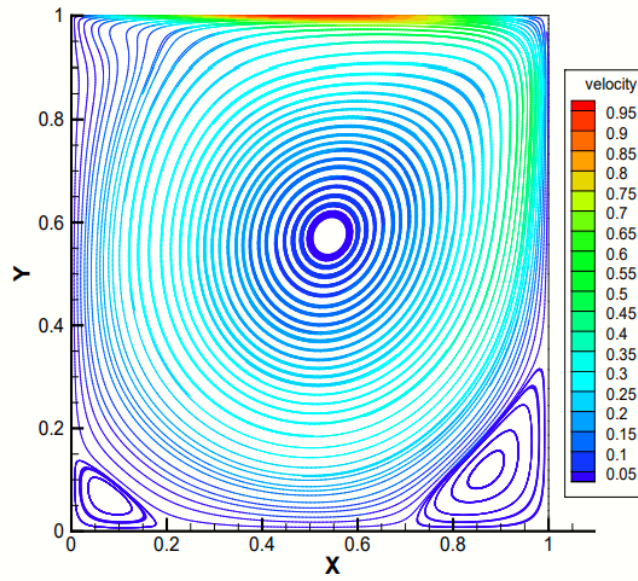


Figure 32: FEA element analysis solution for Reynolds number  $Re = 1000$ .

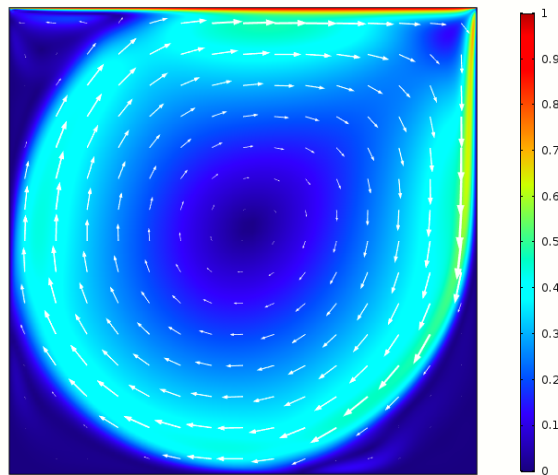


Figure 33: CFD element analysis solution for Reynolds number  $Re = 10000$ .

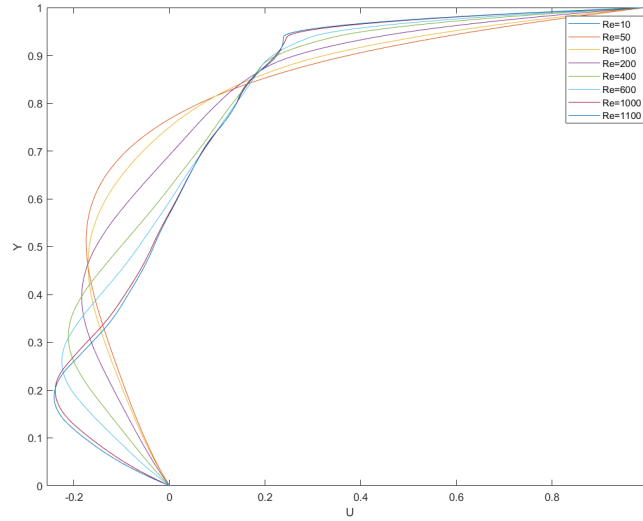


Figure 34: Affect of increasing Reynolds number on axial velocity at  $x=0.5$ .

At this point, the numerical solution is fully validated and implementation is proven quite reliable. Hence, a few applications of this numerical method are discussed next. It should be noted that the proposed platform in IGA considerably reduces the required computational time. For instance, the analyses performed using IGA code for Reynolds number  $Re = 100$  took almost 90 seconds while it took around two hours to solve the same problem using conventional FEA.

## 5 Applications

The developed coupled numerical scheme was used to evaluate the acoustic pressure for 2-d cases. As shown in Fig. 36, we consider a fully developed flow entering a wind tunnel. The tunnel size is 0.4 m in width by 1 m in length and entering velocity  $3.3m/s$ . No slipping boundary conditions were applied at the walls as the pressure remained atmospheric at the exit. For acoustic analyses,

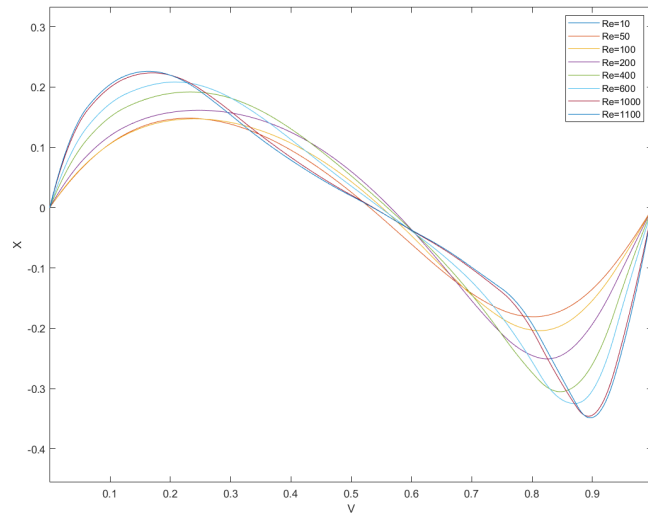


Figure 35: Affect of increasing Reynolds number on normal velocity at  $y = 0.5$  m.

the first-order absorbing boundary was applied at all four sides. The domain mesh is shown in Fig. 37 which is composed of 256 elements.

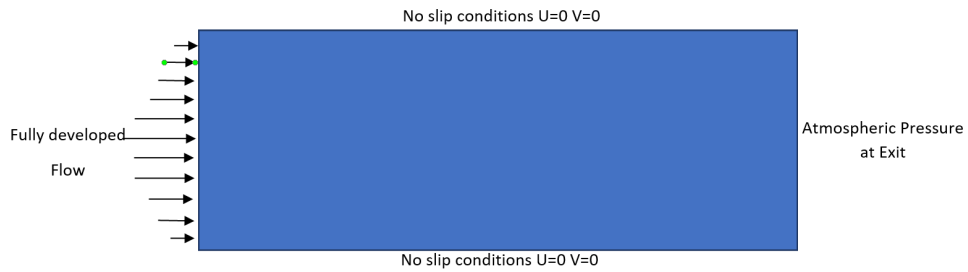


Figure 36: Schematic of wind tunnel problem

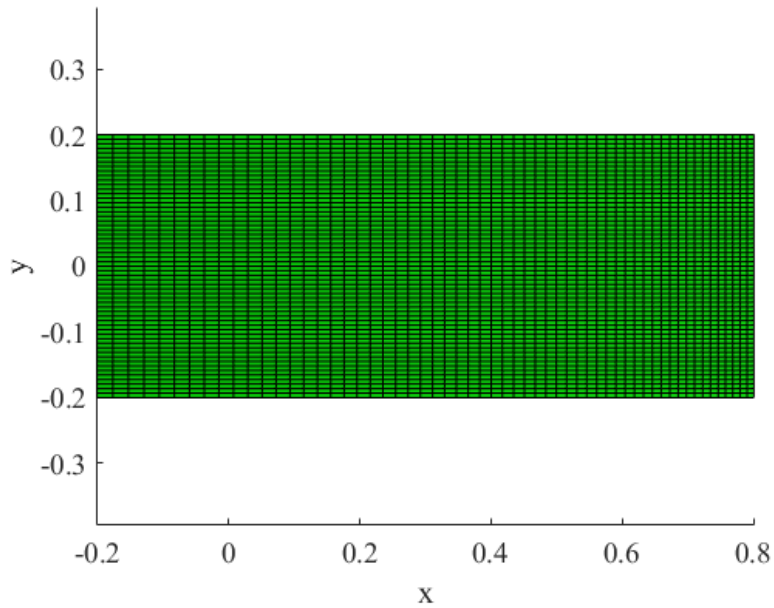


Figure 37: Mesh of wind tunnel problem

## 5.1 Fluid-structure interaction analyses and computation of noise sources

The evolution of the velocity fields is shown in Fig. 38, Fig. 39, and Fig. 40. The turbulence flow is not observed due to the non-existence of any obstacle to urge the flow to act chaotic with a max speed over  $3.5 \text{ m/s}$ . In order to get the harmonic solution, as mentioned before, a Fourier transform is applied to the forces computed at degrees of freedom. The most common frequency was selected, which in this case was  $33\text{hz}$ , to compute the right-hand side of the equation(29). A bigger  $0.8 \times 0.8 \text{ m}$  computational domain was considered to evaluate the acoustic pressure. First, the acoustic forces were transferred from the small domain through interpolation. The acoustic source computed over the extended domain is shown in Fig. 41 and its magnitude is shown in Fig. 42. Then, the acoustic pressure field was calculated using harmonic formulation (equation (29)) and il-

lustrated in Fig. 43 along with pressure amplitude in Fig. 44 which shows a maximum amplitude of about  $0.00052 \text{ pa/m}$  around the entrance of the tunnel.

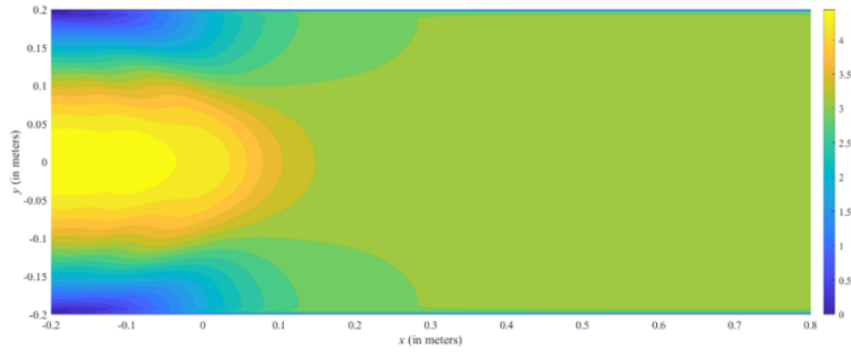


Figure 38: Velocity field at time  $t=0.01$  s for the flow passing through tunnel problem

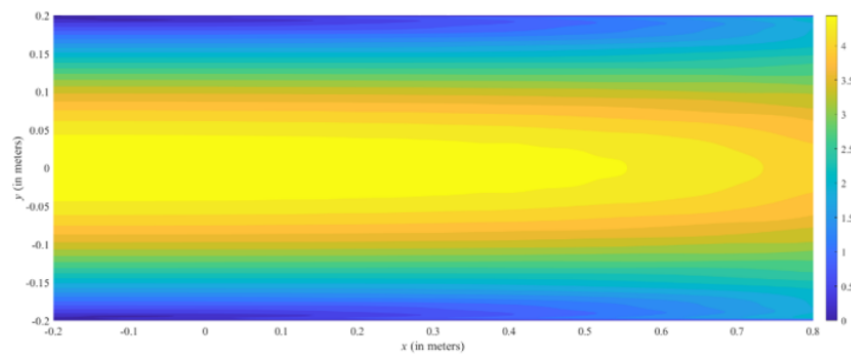


Figure 39: Velocity field at time  $t=0.5$  s for the flow passing through tunnel problem

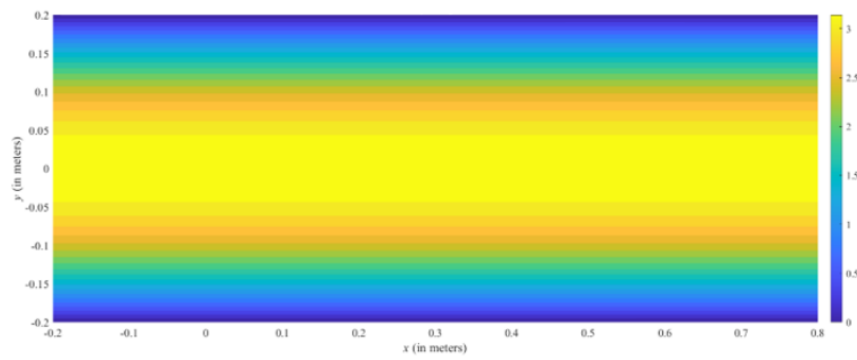


Figure 40: Velocity field at time  $t=1$  s for the flow passing through tunnel problem

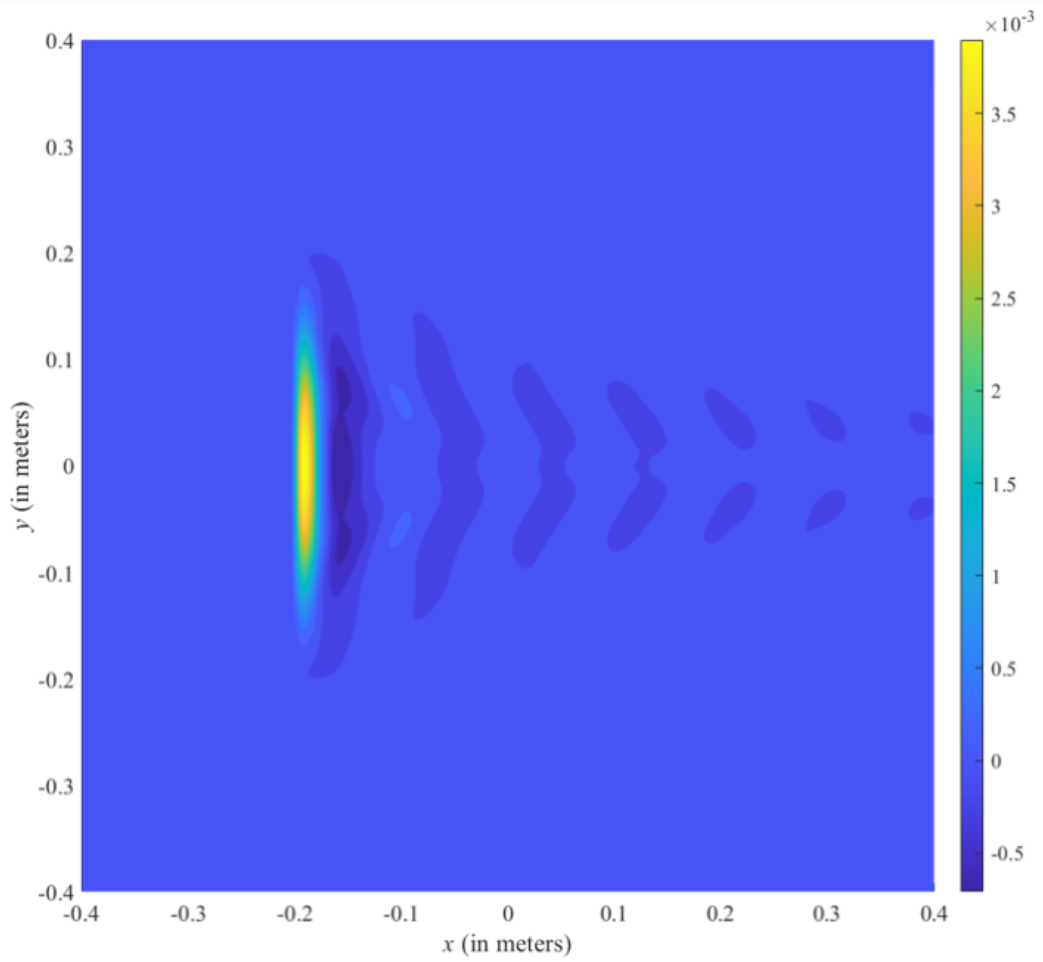


Figure 41: Harmonic acoustic sources generated from flow passing through tunnel

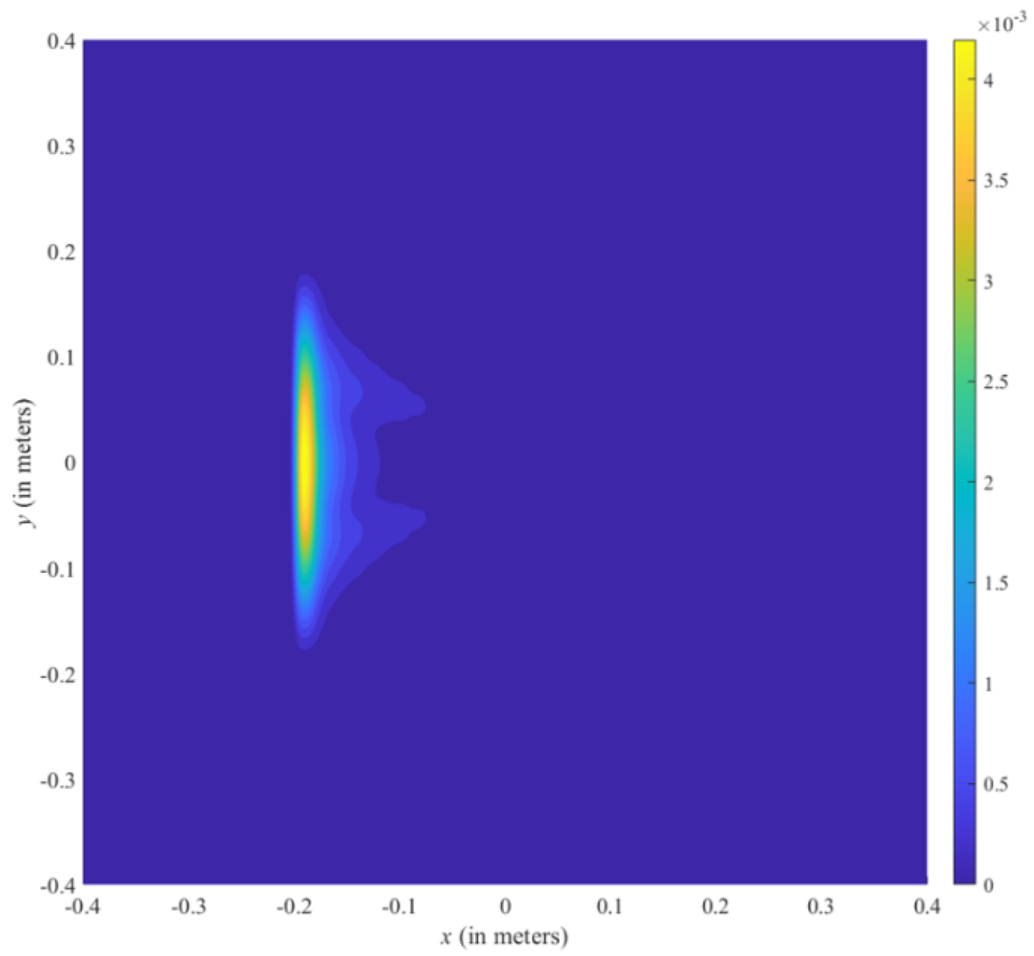


Figure 42: Amplitude of acoustic sources generated from flow passing through tunnel

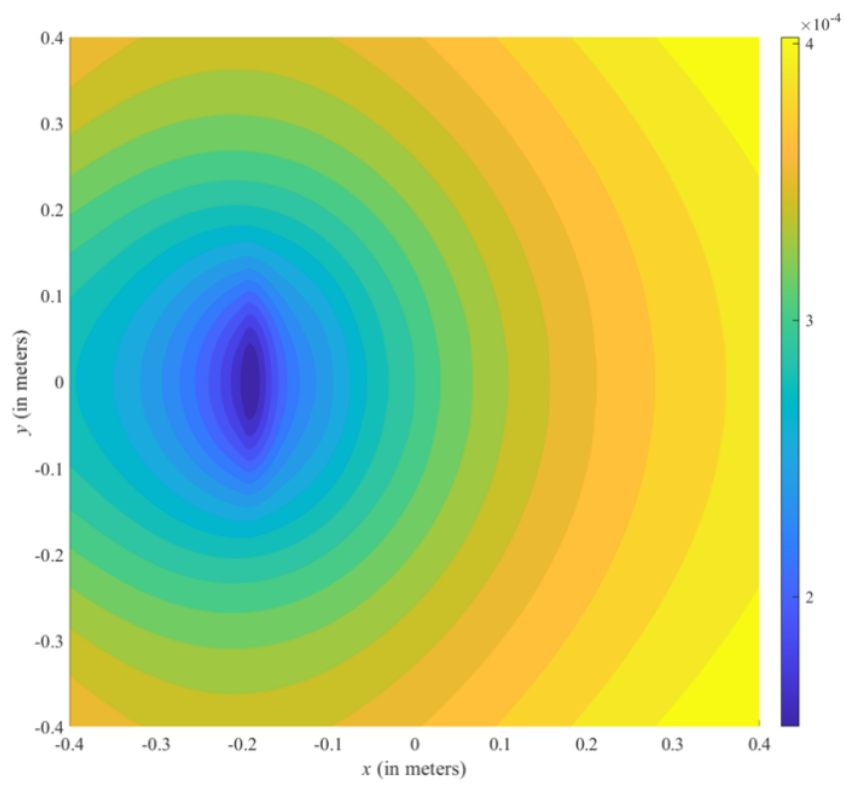


Figure 43: Harmonic acoustic pressure generated from flow passing through tunnel

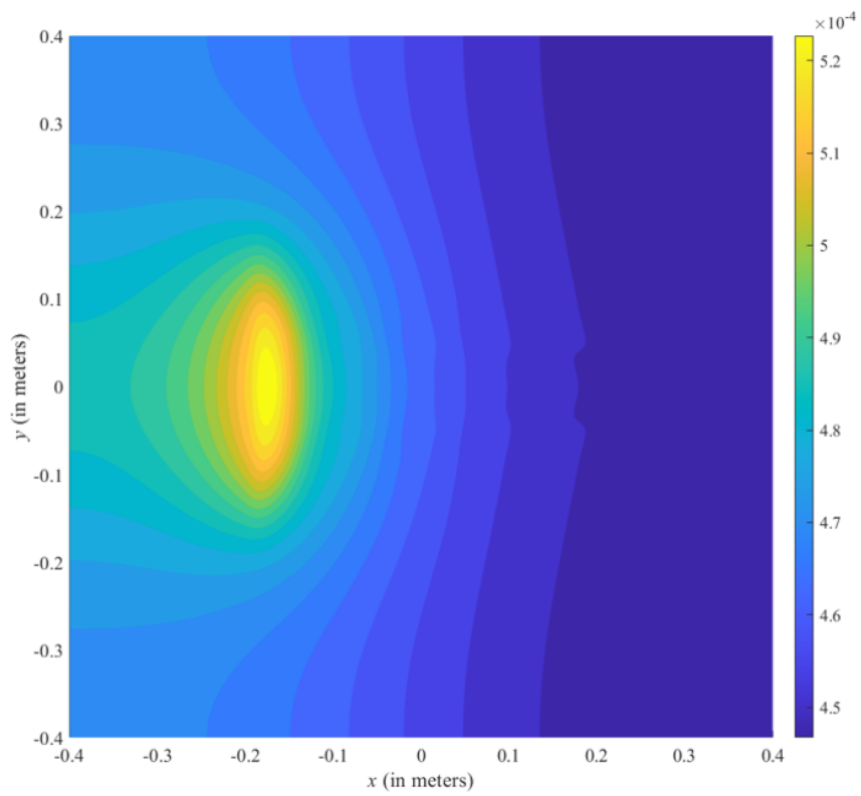


Figure 44: Amplitude of acoustic pressure generated from flow passing through tunnel

## 5.2 The effect of adding an obstacle inside the tunnel

In order to investigate the possibility of noise reduction by adding an acoustic MM it is necessary to examine the effect of adding an obstacle and study its interaction with the flow, compute the noise generated by this obstacle and finally examine the possibility of reducing the noise. We note that adding an obstacle changes the behavior of the fluid, making it more turbulent and most likely increasing the noise levels itself. To illustrate the effects of adding an obstacle upfront to the flow, we are considering adding a cylindrical obstacle, as seen in Fig. 45 with a diameter of  $0.04m$ . The new case has the same boundary conditions stated in the tunnel problem with the addition of added no slipping boundary conditions along the surface of the cylinder. For the meshing aspect, four patches have been used to represent the domain, as shown in Fig. 48a and each patch was composed of about 270 elements.

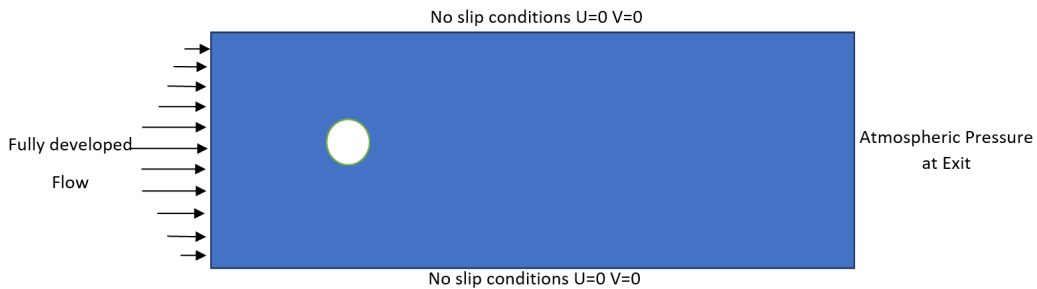
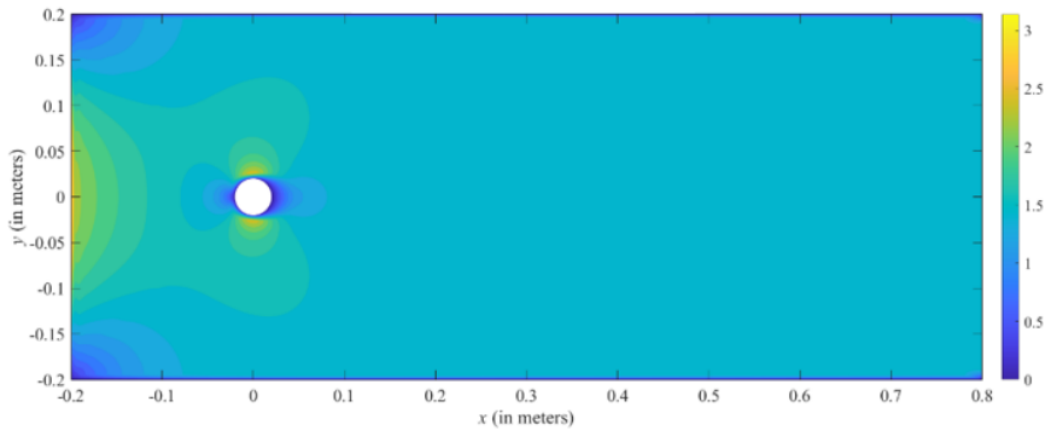
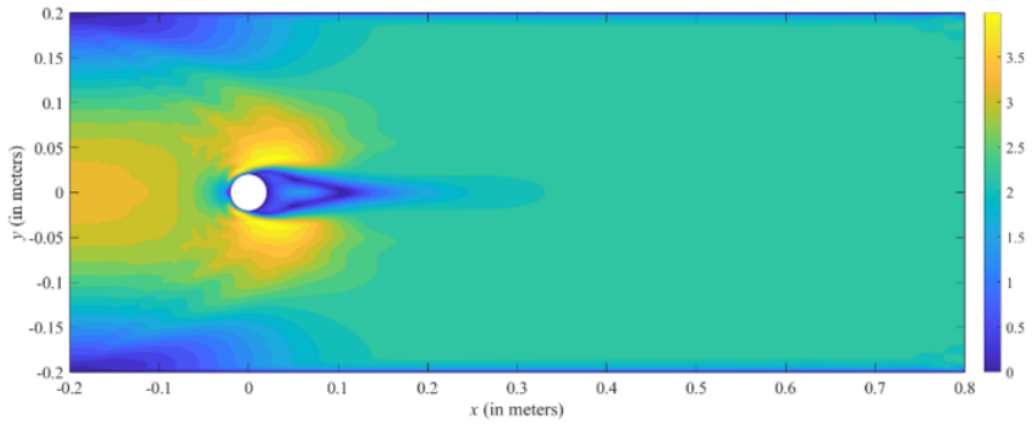


Figure 45: Schematic of wind tunnel problem with cylindrical object

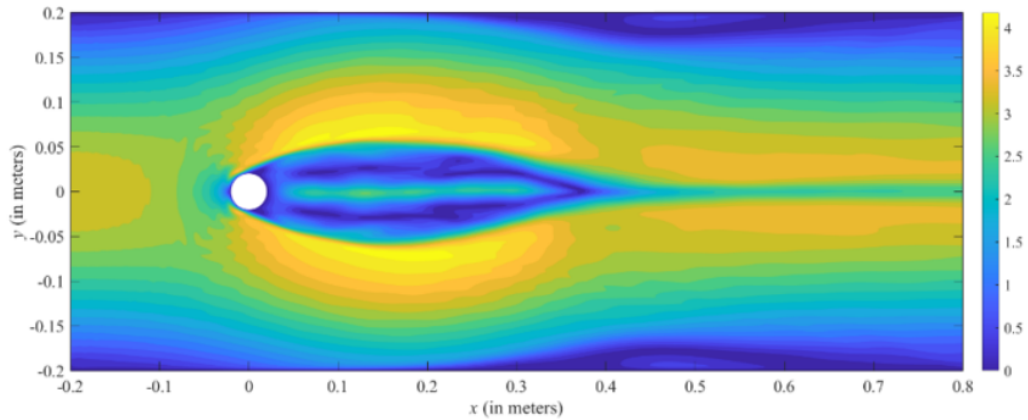
The changes of the velocity field with time are shown in Fig. 46, and Fig. 47 along with the evolution of the vortex behind the cylinder which increases the turbulence of the flow and increases the noise generated.



(a) Velocity distribution at time = 0.001 s



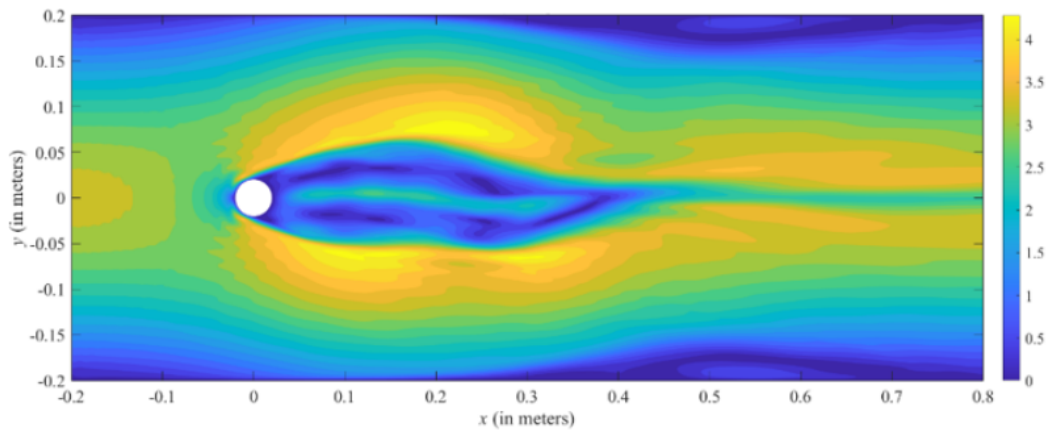
(b) Velocity distribution at time = 0.1 s



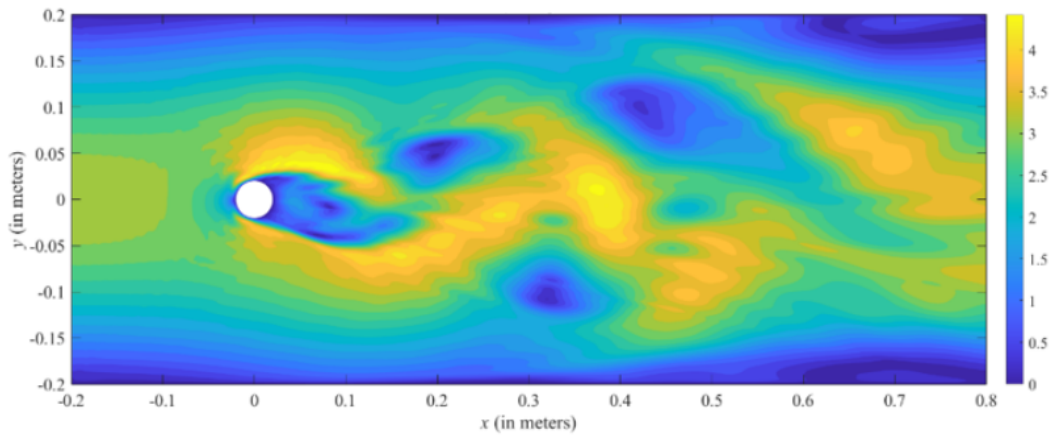
(c) Velocity distribution at time = 1 s

Figure 46: Velocity distribution <sup>72</sup> over time before turbulence starts

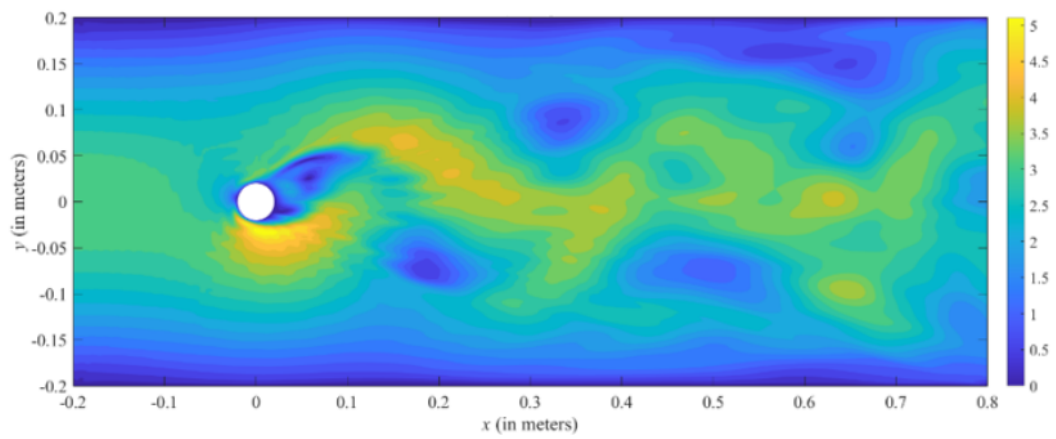
A larger computational domain was used for the harmonic acoustic simulations. The acoustic wave propagation domain was considered to be double the size of the domain used for the velocity field calculations as shown in Fig. 48b. The computed acoustic source was transferred from the old space to the new one with linear interpolating at the degrees of freedom and no additional sources were considered outside the small domain. The acoustic forces calculated using the Lighthill analogy changed considerably with time which was due to adding obstacles. As a case study, a point of  $x = 0.21y = 0$  was selected to observe the effect. As shown in Fig. 49 the acoustic sources started from zero due to the non-existence of velocity. Then they started fluctuating as a result of the development of a vortex. Next, a fast Fourier transfer was applied to the sources for all the degrees of freedom to obtain a harmonic solution; as mentioned before the harmonic solution is considered the most accurate, and less computation-demanding. The real part of the computed harmonic forces is depicted in Fig. 50 which represents the right hands side of the equation (29). Finally, acoustic pressure was computed and the amplitude of the acoustic pressure was depicted in Fig. 51. It can be observed that most of the pressure is generated by the obstacle with a maximum amplitude of  $.0045 Pa/m$ .



(a) Velocity distribution at time = 1.1 s

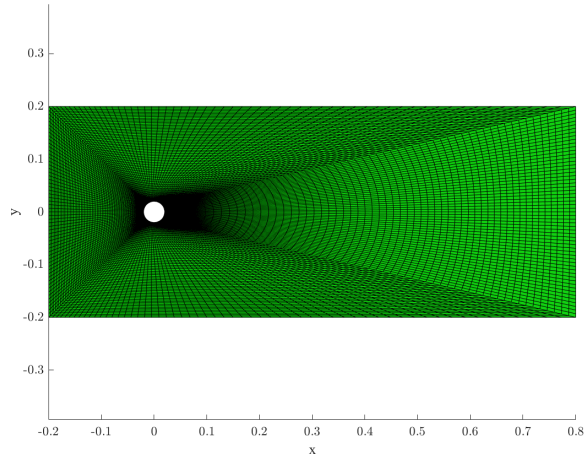


(b) Velocity distribution at time = 1.3 s

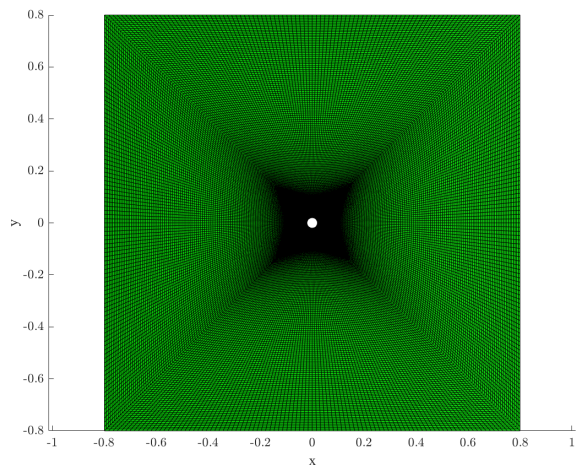


(c) Velocity distribution at time = 1.5 s

Figure 47: Velocity distribution over time after turbulence starts



(a) Mesh used for fluid domain



(b) Mesh used for Acoustic domain

Figure 48: Mesh used for both Fluid and acoustic cases

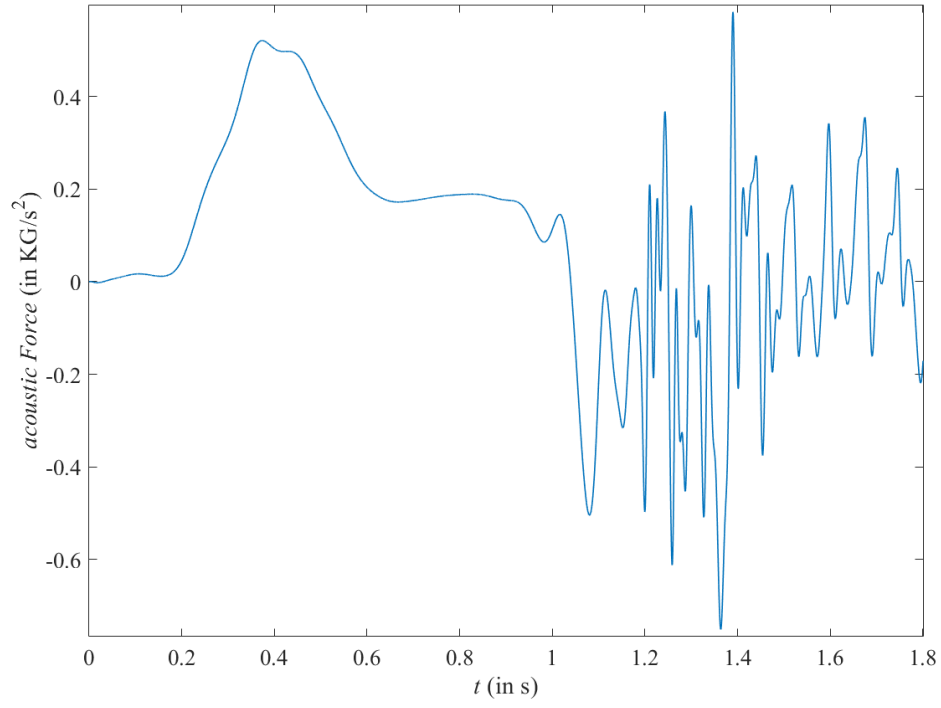


Figure 49: Time domain for acoustic force at point  $x = .21$

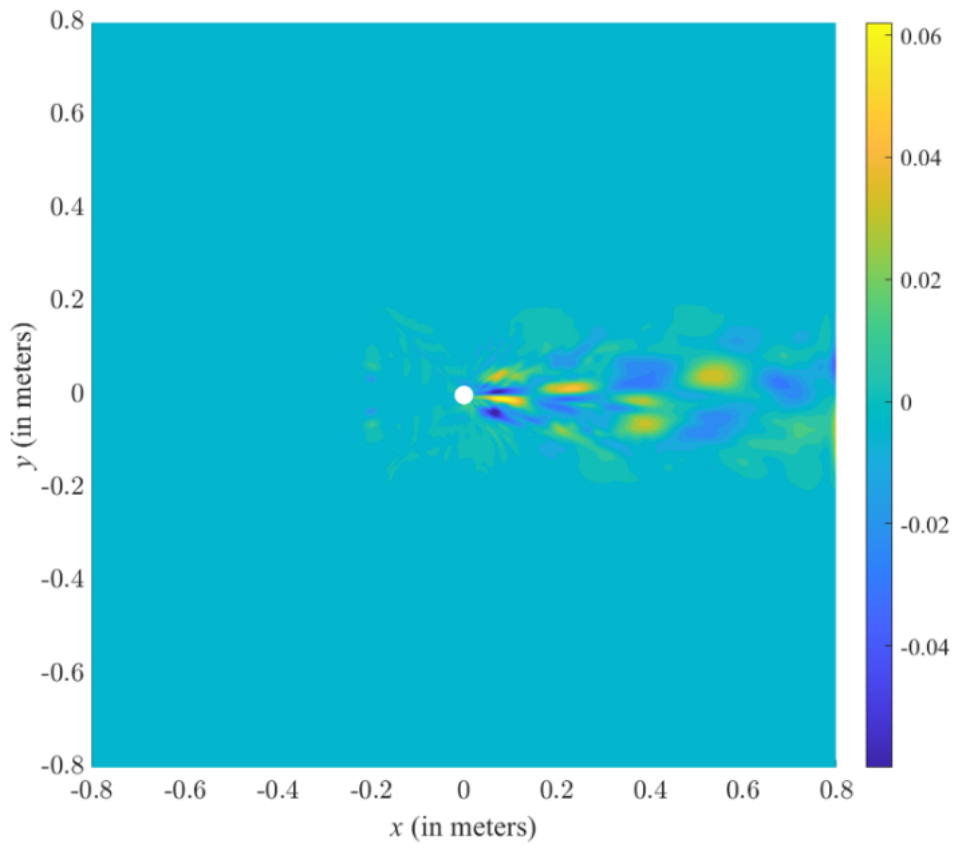


Figure 50: Harmonic noise sources in  $(Kg/s^2)$  for circular object case

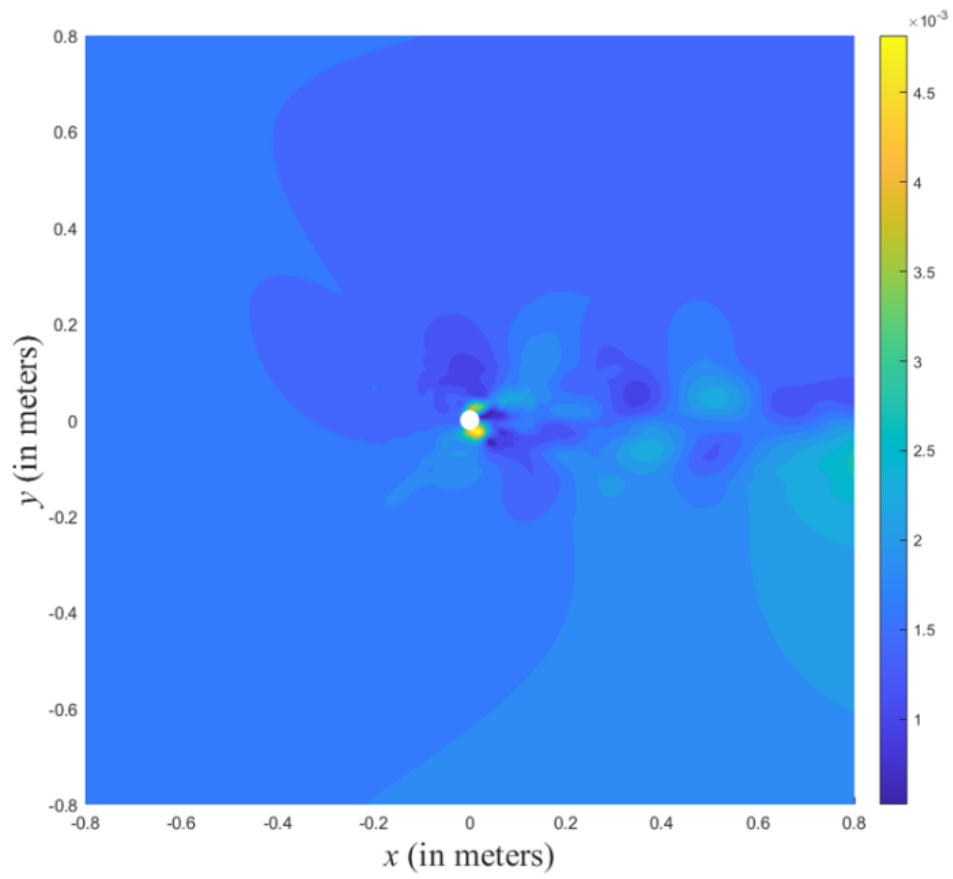


Figure 51: Amplitude of acoustic Pressure( $pa/m$ ) resulting from harmonic solution for circular object case

### 5.3 A metamaterial for aeroacoustic noise reduction

In this section, the possibility of reducing aeroacoustic noise by adding a MM is investigated. First, the cylindrical obstacle is replaced with a tuned MM that works in the same frequency range. The proposed MM has a similar outer shape to a cylinder, as shown in Fig. 52. The selected MM design has a cylindrical outer shape very similar to that of a cylinder. Hence, it is reasonable to assume that velocity fields and the acoustic noise around the MM are the same as those obtained for a cylindrical obstacle. A  $0.4\text{ m}$  radius was considered as the computational domain for the acoustic calculation, as shown in Fig. 53, to ensure that all the sources are included in the calculation. The MM domain was generated using 59 patches. To get the acoustic pressure, first, the sources were transferred to the extended computational domain as shown in Fig. 54. Then, acoustic pressure was computed using equation (29) and its Amplitude is depicted in Fig. 55.

In contrast to the cylinder example, it can be readily observed that the sound pressure is trapped inside the MM and decoupled from the exterior wave. As a result, acoustic pressure was reduced considerably elsewhere, especially when compared with Fig. 50. Finally, to summarize, the axial acoustic pressure is plotted in Fig. 56 for all the cases considered in this study, namely the empty tunnel, the tunnel with a circular object, and the MM. For the cylindrical obstacle, one can detect a periodic change in pressure which is consistent with the evolution of the vortex. The acoustic pressure from the empty tunnel is almost constant. For the MM, however, the analysis shows a decrease in acoustic pressure along the  $x$  - *axis*. This confirms the possibility of aeroacoustic noise reduction using MMs in spite of increased flow fluctuations.

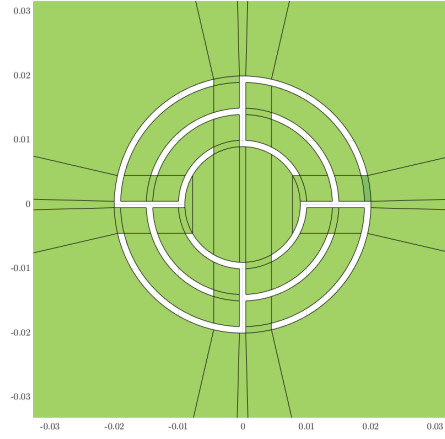


Figure 52: Close image of the acoustic domain that shows the shape of the metamaterial

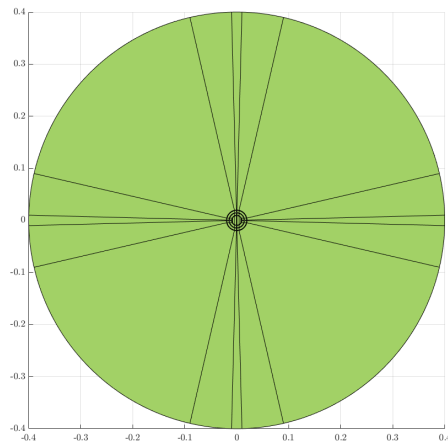


Figure 53: Acoustic domain

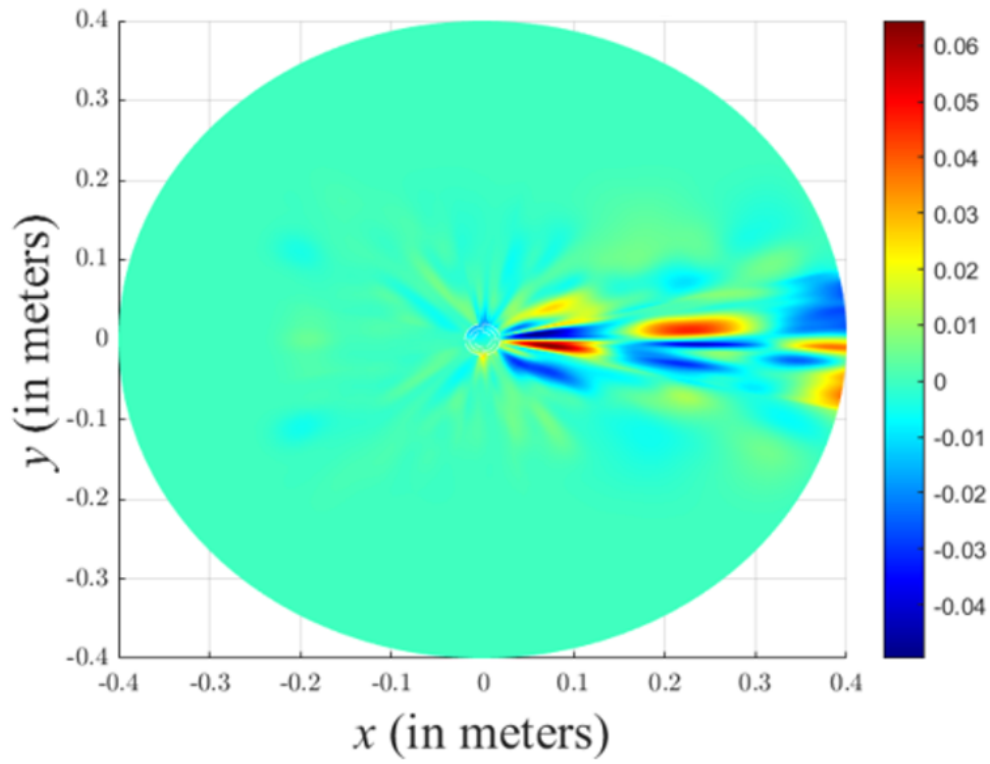


Figure 54: Interpolated acoustic sources( $Kg/s^2$ ) for the metamaterial domain

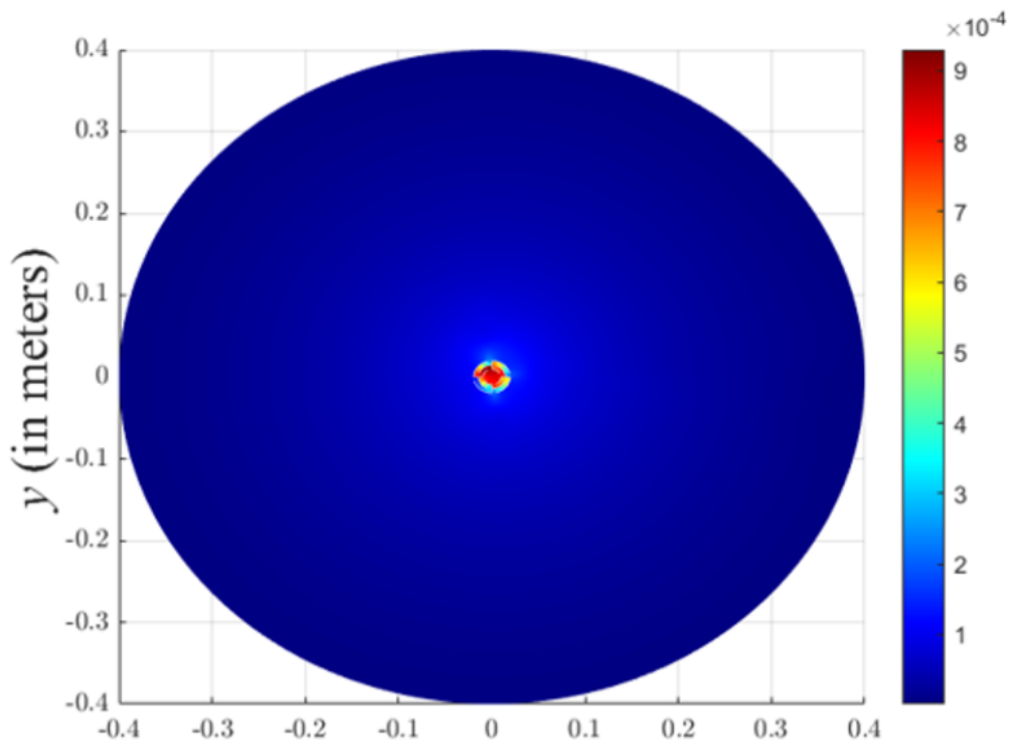


Figure 55: Acoustic pressure amplitude ( $pa/m$ ) domain for the metamaterial

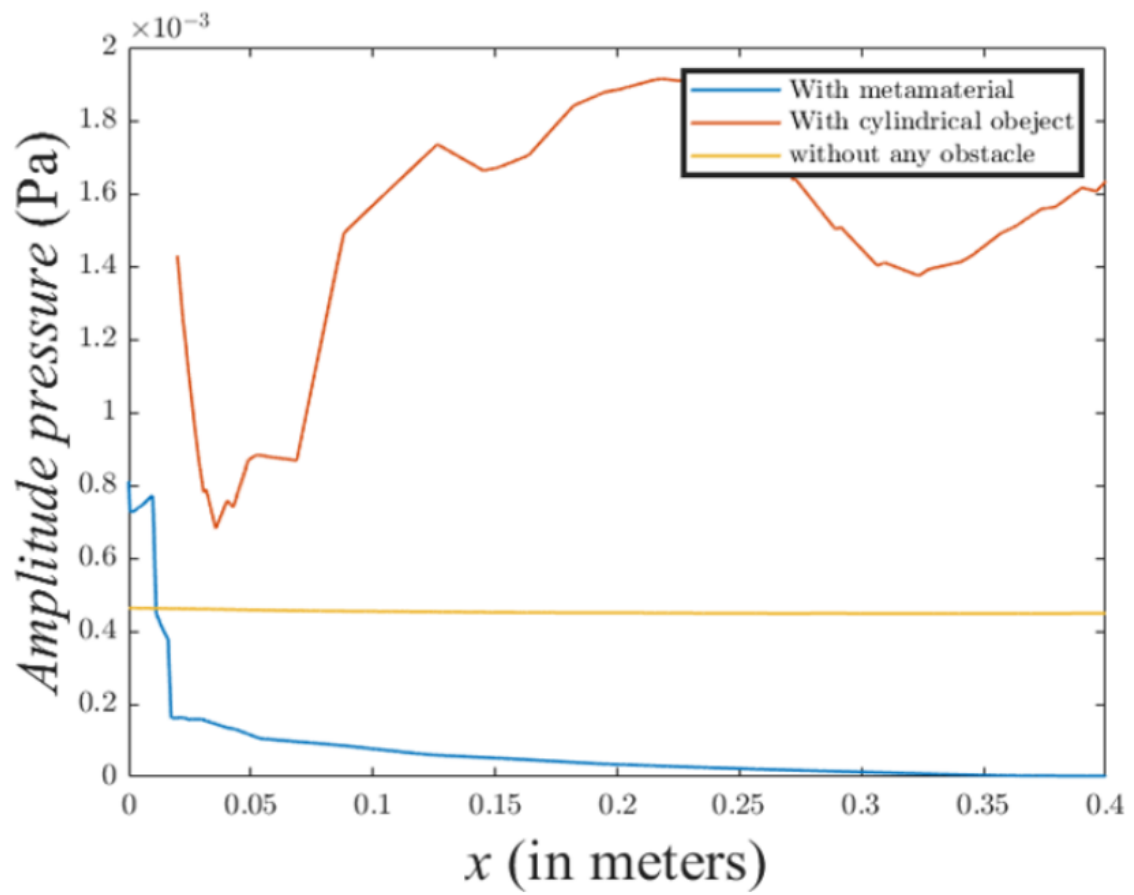


Figure 56: Acoustic pressure amplitude ( $pa/m$ ) along the  $x - axis$  for the three cases

## 6 Conclusions

In this thesis, isogeometric analysis is proven to be a powerful method to perform aeroacoustic analyses offering high accuracy per degree of freedom. The proposed platform also considerably reduced the required computational time when compared with conventional FEA. The pressure stabilized technique was suggested for treating the incompressibility constraint. Stable solutions were obtained, and NURBS interpolation functions were used for all flow variables. Both Newmark and forward schemes were used for time discretization. Lighthill formulation was proposed to evaluate the noise induced by the flow. lid-driven cavity benchmark problem was considered as a means of validation of the proposed platform in solving Navier stokes equations. Co-rotating vortex pair benchmark problem was used to validate the evaluation of acoustic sources. Furthermore, the noise generated by airflow was studied for a tunnel and the effect of adding obstacles was investigated. Finally, it was shown that aeroacoustic noise can be reduced by adding a tuned MM despite increasing the turbulence of the flow field.

Although this thesis provides a numerical tool to predict the noise induced by the interaction of fluid and objects, it doesn't eliminate the need for experimental methods, so experimental validation is recommended as a future study. Moreover, an optimization technique should be developed to design problem-specific MMs. Another possible improvement is the extension of the analyses platform from 2- dimensional to three-dimensional.

## References

- [1] Bolund, P., and Hunhammar, S., 1999. “Ecosystem services in urban areas”. *Ecological economics*, **29**(2), pp. 293–301.
- [2] Muzet, A., 2007. “Environmental noise, sleep and health”. *Sleep medicine reviews*, **11**(2), pp. 135–142.
- [3] Tam, C. K., 2004. “Computational aeroacoustics: an overview of computational challenges and applications”. *International Journal of Computational Fluid Dynamics*, **18**(6), pp. 547–567.
- [4] Afram, A., and Janabi-Sharifi, F., 2014. “Theory and applications of hvac control systems—a review of model predictive control (mpc)”. *Building and Environment*, **72**, pp. 343–355.
- [5] Bennouna, S., Naji, S., Cheriaux, O., Moreau, S., Ouedraogo, B., and Ville, J. M., 2015. Aeroacoustic prediction methods of automotive hvac noise. Tech. rep., SAE Technical Paper.
- [6] Jordan, P., and Gervais, Y., 2008. “Subsonic jet aeroacoustics: associating experiment, modelling and simulation”. *Experiments in Fluids*, **44**(1), pp. 1–21.
- [7] Griffiths, D. V., and Smith, I. M., 2006. *Numerical methods for engineers*. CRC press.
- [8] Alvarez, L., Deriche, R., Sanchez, J., and Weickert, J., 2002. “Dense disparity map estimation respecting image discontinuities: A pde and scale-space based approach”. *Journal of Visual Communication and Image Representation*, **13**(1-2), pp. 3–21.

- [9] Liu, L., Zhang, J., Song, C., Birk, C., and Gao, W., 2019. “An automatic approach for the acoustic analysis of three-dimensional bounded and unbounded domains by scaled boundary finite element method”. *International Journal of Mechanical Sciences*, **151**, pp. 563–581.
- [10] Bazilevs, Y., Beirao da Veiga, L., Cottrell, J. A., Hughes, T. J., and Sangalli, G., 2006. “Isogeometric analysis: approximation, stability and error estimates for h-refined meshes”. *Mathematical Models and Methods in Applied Sciences*, **16**(07), pp. 1031–1090.
- [11] Hosseini, B. S., Möller, M., and Turek, S., 2015. “Isogeometric analysis of the navier–stokes equations with taylor–hood b-spline elements”. *Applied Mathematics and Computation*, **267**, pp. 264–281.
- [12] Hughes, T. J., Cottrell, J. A., and Bazilevs, Y., 2005. “Isogeometric analysis: Cad, finite elements, nurbs, exact geometry and mesh refinement”. *Computer methods in applied mechanics and engineering*, **194**(39-41), pp. 4135–4195.
- [13] Nielsen, P. N., Gersborg, A. R., Gravesen, J., and Pedersen, N. L., 2011. “Discretizations in isogeometric analysis of navier–stokes flow”. *Computer methods in applied mechanics and engineering*, **200**(45-46), pp. 3242–3253.
- [14] Akkerman, I., Bazilevs, Y., Calo, V., Hughes, T., and Hulshoff, S., 2008. “The role of continuity in residual-based variational multiscale modeling of turbulence”. *Computational Mechanics*, **41**(3), pp. 371–378.
- [15] Bazilevs, Y., and Hughes, T., 2008. “Nurbs-based isogeometric analysis for the computation of flows about rotating components”. *Computational Mechanics*, **43**(1), pp. 143–150.

- [16] Hughes, T. J., Franca, L. P., and Hulbert, G. M., 1989. “A new finite element formulation for computational fluid dynamics: Viii. the galerkin/least-squares method for advective-diffusive equations”. *Computer methods in applied mechanics and engineering*, **73**(2), pp. 173–189.
- [17] Cottrell, J. A., Reali, A., Bazilevs, Y., and Hughes, T. J., 2006. “Isogeometric analysis of structural vibrations”. *Computer methods in applied mechanics and engineering*, **195**(41-43), pp. 5257–5296.
- [18] Beirão da Veiga, L., Buffa, A., Rivas, J., and Sangalli, G., 2011. “Some estimates for h–p–k-refinement in isogeometric analysis”. *Numerische Mathematik*, **118**(2), pp. 271–305.
- [19] Xu, G., Li, B., Shu, L., Chen, L., Xu, J., and Khajah, T., 2019. “Efficient  $r$ -adaptive isogeometric analysis with Winslow’s mapping and monitor function approach”. *Journal of Computational and Applied Mathematics*, **351**, pp. 186–197.
- [20] Cottrell, J., Hughes, T., and Reali, A., 2007. “Studies of refinement and continuity in isogeometric structural analysis”. *Computer methods in applied mechanics and engineering*, **196**(41-44), pp. 4160–4183.
- [21] Khajah, T., Antoine, X., and Bordas, S. P. A., 2019. “B-spline FEM for time-harmonic acoustic scattering and propagation”. *Journal of Theoretical and Computational Acoustics*, **27**(03), p. 1850059.
- [22] Lighthill, M. J., 1952. “On sound generated aerodynamically i. general theory”. *Proceedings of the Royal Society of London. Series A. Mathematical and Physical Sciences*, **211**(1107), pp. 564–587.

- [23] Lighthill, M. J., 1954. “On sound generated aerodynamically ii. turbulence as a source of sound”. *Proceedings of the Royal Society of London. Series A. Mathematical and Physical Sciences*, **222**(1148), pp. 1–32.
- [24] Ffowcs Williams, J. E., and Hawkings, D. L., 1969. “Sound generation by turbulence and surfaces in arbitrary motion”. *Philosophical Transactions of the Royal Society of London. Series A, Mathematical and Physical Sciences*, **264**(1151), pp. 321–342.
- [25] Khajah, T., Antoine, X., and Bordas, S. P. A., 2016. Isogeometric finite element analysis of time-harmonic exterior acoustic scattering problems.
- [26] Videla, J., Anitescu, C., Khajah, T., Bordas, S., and Atroshchenko, E., 2019. “ $h$ - and  $p$ -adaptivity driven by recovery and residual-based error estimators for PHT-splines applied to time-harmonic acoustics”. *Computers and Mathematics with Applications*, **77**(9), pp. 2369–2395.
- [27] Khajah, T., and Villamizar, V., 2019. “Highly accurate acoustic scattering: Isogeometric Analysis coupled with local high order Farfield Expansion ABC”. *Computer Methods in Applied Mechanics and Engineering*, **349**, pp. 477–498.
- [28] Villamizar, V., Khajah, T., Acosta, S., Grundvig, D., Badger, J., and Rojas, O., 2020. “High order local absorbing boundary conditions for acoustic and elastic scattering”. *The Journal of the Acoustical Society of America*, **148**(4), pp. 2451–2451.
- [29] Dsouza, S., Khajah, T., Antoine, X., Bordas, S., and Natarajan, S., 2021. “Non Uniform Rational B-Splines and Lagrange approximations for time-harmonic acoustic scattering: accu-

- racy and absorbing boundary conditions”. *Mathematical and Computer Modelling of Dynamical Systems*, **27**(1), pp. 263–294.
- [30] Antoine, X., and Khajah, T., 2022. “Standard and phase reduced isogeometric on-surface radiation conditions for acoustic scattering analyses”. *Computer Methods in Applied Mechanics and Engineering*, **392**, p. 114700.
- [31] Atroshchenko, E., Calderon Hurtado, A., Anitescu, C., and Khajah, T., 2022. “Isogeometric collocation for acoustic problems with higher-order boundary conditions”. *Wave Motion*, **110**, p. 102861.
- [32] Ummidivarapu, V., Voruganti, H., Khajah, T., and Bordas, S., 2020. “Isogeometric shape optimization of an acoustic horn using the teaching-learning-based optimization (tlbo) algorithm”. *Computer Aided Geometric Design*, **80**, p. 101881.
- [33] Dodgen, G., and Khajah, T., 2019. “Effectiveness of Tikhonov Smoothing in isogeometric shape optimization of the horn speaker”. *ASEE-GSW*.
- [34] Dodgen, G., and Khajah, T., 2018. “Shape optimization of an acoustic horn using differential evolution and isogeometric analysis”. In IGA 2018 Conference, Austin, Texas.
- [35] Dodgen, G., and Khajah, T., 2019. “Effectiveness of Tikhonov smoothing in isogeometric shape optimization of the horn speaker”. In ASEE conference, Tyler, TX.
- [36] Khajah, T., Liu, L., Song, C., and Gravenkamp, H., 2021. “Shape optimization of acoustic devices using the scaled boundary finite element method”. *Wave Motion*, **104**, p. 102732.

- [37] Gomez, H., Hughes, T. J., Nogueira, X., and Calo, V. M., 2010. “Isogeometric analysis of the isothermal navier–stokes–korteweg equations”. *Computer Methods in Applied Mechanics and Engineering*, **199**(25-28), pp. 1828–1840.
- [38] Sigalas, M. M., and Economou, E. N., 1992. “Elastic and acoustic wave band structure”. *Journal of sound and vibration*, **158**(2), pp. 377–382.
- [39] Smith, D. R., Padilla, W. J., Vier, D., Nemat-Nasser, S. C., and Schultz, S., 2000. “Composite medium with simultaneously negative permeability and permittivity”. *Physical review letters*, **84**(18), p. 4184.
- [40] Liu, X., Tyler, T., Starr, T., Starr, A. F., Jokerst, N. M., and Padilla, W. J., 2011. “Taming the blackbody with infrared metamaterials as selective thermal emitters”. *Physical review letters*, **107**(4), p. 045901.
- [41] Zheng, X., Lee, H., Weisgraber, T. H., Shusteff, M., DeOtte, J., Duoss, E. B., Kuntz, J. D., Biener, M. M., Ge, Q., Jackson, J. A., et al., 2014. “Ultralight, ultrastiff mechanical metamaterials”. *Science*, **344**(6190), pp. 1373–1377.
- [42] Hao, J., Wang, J., Liu, X., Padilla, W. J., Zhou, L., and Qiu, M., 2010. “High performance optical absorber based on a plasmonic metamaterial”. *Applied Physics Letters*, **96**(25), p. 251104.
- [43] Liu, Z., Zhang, X., Mao, Y., Zhu, Y., Yang, Z., Chan, C. T., and Sheng, P., 2000. “Locally resonant sonic materials”. *science*, **289**(5485), pp. 1734–1736.

- [44] Torrent, D., and Sánchez-Dehesa, J., 2008. “Acoustic cloaking in two dimensions: a feasible approach”. *New Journal of Physics*, **10**(6), p. 063015.
- [45] Liang, Z., and Li, J., 2012. “Extreme acoustic metamaterial by coiling up space”. *Physical review letters*, **108**(11), p. 114301.
- [46] Wei, W., Ren, S., Chronopoulos, D., and Meng, H., 2021. “Optimization of connection architectures and mass distributions for metamaterials with multiple resonators”. *Journal of Applied Physics*, **129**(16), p. 165101.
- [47] Man, X., Liu, T., Xia, B., Luo, Z., Xie, L., and Liu, J., 2018. “Space-coiling fractal metamaterial with multi-bandgaps on subwavelength scale”. *Journal of Sound and Vibration*, **423**, pp. 322–339.
- [48] Galdi, G., 2011. *An introduction to the mathematical theory of the Navier-Stokes equations: Steady-state problems*. Springer Science & Business Media.
- [49] Tu, J., Yeoh, G. H., and Liu, C., 2018. *Computational fluid dynamics: a practical approach*. Butterworth-Heinemann.
- [50] Ferziger, J. H., Perić, M., and Street, R. L., 2002. *Computational methods for fluid dynamics*, Vol. 3. Springer.
- [51] Bastl, B., Brandner, M., Egermaier, J., Horníková, H., Michálková, K., and Turnerová, E., 2021. “Numerical simulation of lid-driven cavity flow by isogeometric analysis”. *Acta Polytechnica*, **61**(SI), pp. 33–48.

- [52] Hirsch, C., 1990. “Numerical computation of internal and external flows. vol. 2-computational methods for inviscid and viscous flows”. *Chichester*.
- [53] Bhutta, M. M. A., Hayat, N., Bashir, M. H., Khan, A. R., Ahmad, K. N., and Khan, S., 2012. “Cfd applications in various heat exchangers design: A review”. *Applied Thermal Engineering*, **32**, pp. 1–12.
- [54] Droniou, J., 2014. “Finite volume schemes for diffusion equations: introduction to and review of modern methods”. *Mathematical Models and Methods in Applied Sciences*, **24**(08), pp. 1575–1619.
- [55] Lee, J. K., and Froehlich, D. C., 1987. “Review of literature on the finite-element solution of the equations of two-dimensional surface-water flow in the horizontal plane”.
- [56] Scardovelli, R., and Zaleski, S., 1999. “Direct numerical simulation of free-surface and interfacial flow”. *Annual review of fluid mechanics*, **31**(1), pp. 567–603.
- [57] Coleman, G. N., and Sandberg, R. D., 2010. “A primer on direct numerical simulation of turbulence-methods, procedures and guidelines”.
- [58] Ewert, R., and Emunds, R., 2005. “Caa slat noise studies applying stochastic sound sources based on solenoidal digital filters”. In 11th AIAA/CEAS aeroacoustics conference, p. 2862.
- [59] Nagarajan, S., Hahn, S., and Lele, S., 2006. “Prediction of sound generated by a pitching airfoil: a comparison of rans and les”. In 12th AIAA/CEAS Aeroacoustics Conference (27th AIAA Aeroacoustics Conference), p. 2516.

- [60] Lummer, M., Delfs, J., and Lauke, T., 2002. “Simulation of sound generation by vortices passing the trailing edge of airfoils”. In 8th AIAA/CEAS Aeroacoustics Conference & Exhibit, p. 2578.
- [61] Yusuf, S. N. A., Asako, Y., Sidik, N. A. C., Mohamed, S. B., and Japar, W. M. A. A., 2020. “A short review on rans turbulence models”. *CFD Letters*, **12**(11), pp. 83–96.
- [62] Ayhan, H., and Sökmen, C. N., 2012. “Cfd modeling of thermal mixing in a t-junction geometry using les model”. *Nuclear Engineering and Design*, **253**, pp. 183–191.
- [63] Mueller, M. E., and Pitsch, H., 2012. “Les model for sooting turbulent nonpremixed flames”. *Combustion and Flame*, **159**(6), pp. 2166–2180.
- [64] Wagner, C., Hüttl, T., and Sagaut, P., 2007. *Large-eddy simulation for acoustics*, Vol. 20. Cambridge University Press.
- [65] Tezduyar, T. E., 1991. “Stabilized finite element formulations for incompressible flow computations”. *Advances in applied mechanics*, **28**, pp. 1–44.
- [66] Droux, J.-J., and Hughes, T. J., 1994. “A boundary integral modification of the galerkin least squares formulation for the stokes problem”. *Computer methods in applied mechanics and engineering*, **113**(1-2), pp. 173–182.
- [67] Escobar, M., 2007. *Finite element simulation of flow-induced noise using Lighthill’s acoustic analogy*. Friedrich-Alexander-Universitaet Erlangen-Nuernberg (Germany).
- [68] Chang, S.-Y., 2004. “Studies of newmark method for solving nonlinear systems:(i) basic analysis”. *Journal of the Chinese Institute of Engineers*, **27**(5), pp. 651–662.

- [69] Schinnerl, M., Kaltenbacher, M., Langer, U., Lerch, R., and Schöberl, J., 2007. “A survey in mathematics for industry an efficient method for the numerical simulation of magneto-mechanical sensors and actuators”. *European Journal of Applied Mathematics*, **18**(2), pp. 233–271.
- [70] Duhamel, D., and Nguyen, T.-M., 2009. “Finite element computation of absorbing boundary conditions for time-harmonic wave problems”. *Computer methods in applied mechanics and engineering*, **198**(37-40), pp. 3006–3019.
- [71]
- [72] Schwartzkopff, T., 2005. “High-order finite volume methods and heterogeneous domain decomposition for numerical aeroacoustics”.
- [73] Lee, D. J., and Koo, S. O., 1995. “Numerical study of sound generation due to a spinning vortex pair”. *AIAA Journal*, **33**(1), pp. 20–26.
- [74] Ewert, R., and Schröder, W., 2003. “Acoustic perturbation equations based on flow decomposition via source filtering”. *Journal of Computational Physics*, **188**(2), pp. 365–398.
- [75] PETERS, M., 1993. “Aeroacoustic sources in internal flows(ph. d. thesis)”.
- [76] Scully, M., 1975. “Computation of helicopter rotor wake geometry and its influence on rotor harmonic airloads”. PhD thesis, Massachusetts Institute of Technology.
- [77] Bhagwat, M. J., and Leishman, J. G., 2002. “Generalized viscous vortex model for application to free-vortex wake and aeroacoustic calculations”. In Annual forum proceedings-American helicopter society, Vol. 58, American Helicopter Society, Inc, pp. 2042–2057.

- [78] Müller, E., and Obermeier, F., 1967. “The spinning vortices as a source of sound”. *AGARD CP-22*, pp. 22–1.
- [79] Elhanafy, A., Guaily, A., and Elsaid, A., 2017. “Pressure stabilized finite elements simulation for steady and unsteady newtonian fluids”. *Journal of Applied Mathematics and Computational Mechanics*, **16**(3), pp. 17–26.
- [80] Hirsch, C., 2007. *Numerical computation of internal and external flows: The fundamentals of computational fluid dynamics*. Elsevier.
- [81] Ghia, U., Ghia, K. N., and Shin, C., 1982. “High-re solutions for incompressible flow using the navier-stokes equations and a multigrid method”. *Journal of computational physics*, **48**(3), pp. 387–411.